RAREFIED FLOW

James N. Moss

Aerothermodynamics Branch
Aerodynamics and Gas Dynamics Division
NASA Langley Research Center
Hampton, VA 23681-0001
USA

and

Jean-Claude Lengrand

Laboratoire d'Aérothermique du
CNRS
4 ter, route des gardes
92190 Meudon
FRANCE

CONTENTS

1   INTRODUCTION

Rarefaction effects are important for hypersonic applications for a wide spectrum of conditions ranging from low-density (high altitude) situations to relatively high-density flows where the characteristic dimension is small. The present chapter concentrates on two hypersonic flow problems at flow conditions that produce a significant range of rarefaction effects: corner flow with jet interaction and blunt body flow with special emphasis on the near wake. These problems were chosen because they involve complex flow interactions that have significant implications for both spacecraft and re-entry vehicles. In an effort to clarify issues associated with these two general flow problems and to enhance their respective databases, both experimental and computational contributions were executed by an international group of researchers. In some cases, multiple data sources for both experimental and computational contributions are achieved. The Phase I report of WG 18[1] (Chapter IV) provides an overview of the accomplishments and plans of this activity as of early 1994.

The corner flow jet interaction problem was incorporated to provide data to enhance our understanding of the forces

generated on surfaces as a result of the interaction between reaction control system (RCS) exhaust plumes and the flow field surrounding a vehicle. Most space vehicles are controlled with reaction thrusters during atmospheric entry. These RCS jets can be used independently or in conjunction with movable aerodynamic surfaces, depending on the specific vehicle configuration and flight conditions. The exhaust plumes of the control jets act as barriers to the external flow, creating an effect that can change the pressure distribution along the vehicle surface containing the jet, as well as on surfaces surrounding the exhaust plume. The surface pressure perturbations from the jet interaction must be accurately predicted in order to obtain the desired vehicle aerodynamic performance.

The use of RCS jets becomes vital at higher altitudes where the density is low enough to render the control surfaces ineffective. As the altitude increases and the free-stream flow becomes more rarefied, the level of interaction between the control jet and the free stream diminishes and is practically nonexistent when the free-stream mean free path is very large. Therefore, it is crucial to accurately model RCS firings at intermediate altitudes where reaction controls are needed and significant control jet interactions are expected.

In an effort to gain further insight into the control jet interaction problem, an experimental[2-4] study was conducted by the European Space Agency (ESA) at the SR3 low-density wind tunnel of CNRS in Meudon, France. The principal measurements were surface pressure for a matrix of free-stream and jet flow conditions with nitrogen as the test gas for the free stream and jet.

Subsequent to the SR3 experiment, numerical studies were conducted at Aerospatiale[5], CNRS[6], and NASA Langley[7-9] using both direct simulation Monte Carlo (DSMC) and Navier-Stokes computational tools. These are believed to be the first computational studies for this type of complex three-dimensional problem with both rarefied and continuum components, i.e., the rarefied external flow interaction with a jet whose central core is at continuum conditions.

The second problem concerns blunt body flows and their wake closure, which is important for planetary probes and aerobrake configurations. Wake closure is a critical issue for aerobrakes because the low lift-to-drag ratio aeroshell designs impose constraints on payload configuration/spacecraft design. The issue is that the payload must fit into the wake flow to minimize heating because high heating rates are generally associated with reattachment of the separated near-wake flows.

A number of fundamental questions exist concerning such flows: How does the wake structure change as a function of rarefaction? What role does thermochemical nonequilibrium play in the near-wake structure? To what limits are continuum models realistic as rarefaction in the wake is progressively increased? Answers to these fundamental questions are needed because the potential for rarefaction effects on wake structure exists for much of an aerobraking maneuver. Note that the expansion of even continuum forebody flow into the near wake can result in relatively large local Knudsen numbers.

The experimental test plan for this problem consisted of two parts: one is the high-enthalpy tests obtained with impulse facilities complemented with perfect gas wind tunnel data (discussed in Chapter IV) and the second is tests at intermediate- to high-Knudsen-number conditions. The rarefied tests were performed primarily in low-enthalpy facilities with chemically inert conditions. In addition, tests were conducted in two impulse facilities at either low pressure conditions or with very small models to capture both real gas and rarefaction effects. The same forebody model configuration was used for all tests—a 70° spherically blunted cone—and is the same as that for the Mars Pathfinder Probe[10]. Mars Pathfinder was launched in December 1996 and made a successful entry, descent, and landing July 4, 1997.

The rarefied experiments were performed in five facilities: four in Europe and one in the U.S. For all of the tests performed, the Knudsen number based on free-stream mean free path and model base diameter was of the order of 0.001 or larger. The database from these studies includes aerodynamics (C_L, C_D, C_m, and the center of pressure); local surface heating rate along the forebody, base plane, and sting; and wake structure as inferred from density and velocity measurements in the near wake. The model was supported either by sting or wires.

Extensive calculations at these experimental test conditions have been performed using DSMC and Navier-Stokes solvers. The computational results are compared with selected experimental results and code-to-code comparisons are made for a few test cases. Computational findings help clarify the boundaries for realistic application of Navier-Stokes algorithms with respect to rarefaction effects. Also, the potential for application of hybrid DSMC/Navier Stokes solvers to the blunt body wake problem was explored. By expanding the computational problems to include high altitude flight conditions, an assessment of the combined effects of rarefaction and thermochemical nonequilibrium on wake structure is made. Two flight conditions are examined: one in the Earth's atmosphere and one in the Mars atmosphere, both at the same free-stream velocity (7 km/s) and number density ($1.654 \times 10^{20} \text{m}^{-3}$) and for the same forebody configuration with a base diameter of 2 meters.

2 TEST-CASE DEFINITION

Two experimental test cases have been investigated. The corner-flow/jet interaction test model is used to analyze

transverse flows interacting with walls and with external rarefied hypersonic flows. The blunt-body/wake closure test model is investigated to characterize the wake structure and aerothermal loads at different rarefaction levels of the external hypersonic flow.

The corner-flow/jet interaction problem is complicated because it combines the corner flow problem (often studied as a simplification of the wing-fuselage junction problem) with jet interaction. A bibliographic study of this problem reveals that

- it has been widely studied in the past with a major application to space vehicles and missiles;

- the approach was based on a combination of experimental results and similarity considerations;

- co-flowing and counter-flowing configurations have been studied more than transverse injection; however transverse injection has been studied for application to SCRAMJET engines (low external Mach number, no rarefaction, important role of turbulence);

- predictive methods adapted to the problem of jet/flow interaction require validation for each particular case, and generally they do not account for rarefaction effects;

- general methods (solving Navier-Stokes equations, DSMC, and hybrid DSMC/Navier-Stokes) are candidates for solving the problem but face difficulties due to severe gradients and to the simultaneous presence of dense and rarefied zones.

The blunt-body wake-closure problem involves complex flow interactions resulting from the compressive forebody flow undergoing a rapid expansion into the wake and its associated shear layer reattachment process. Existing data bases for the rarefied flow regime were quite sparse from both the experimental and computational perspectives at the outset of the WG 18 activity.

2.1 Experimental

2.1.1 Corner-Flow / Jet Interaction

As shown in Fig. 1, the corner-flow model is made of two perpendicular flat plates with sharp leading edges. The intersection of the two plates is oriented in the direction of the external free stream. A transverse jet is issued from a supersonic nozzle located in the horizontal plate. This jet interacts with the external flow (part (a) of Table 1) and with the surrounding surfaces.

2.1.2 Blunt-Body / Wake-Closure Test Model

The blunt body is an axisymmetric ASTV (Aeroassist Space Transfer Vehicle) type model. Depending upon the test facility and the type of measurement, models were supported by either stings or wires. For the sting-mounted models, the
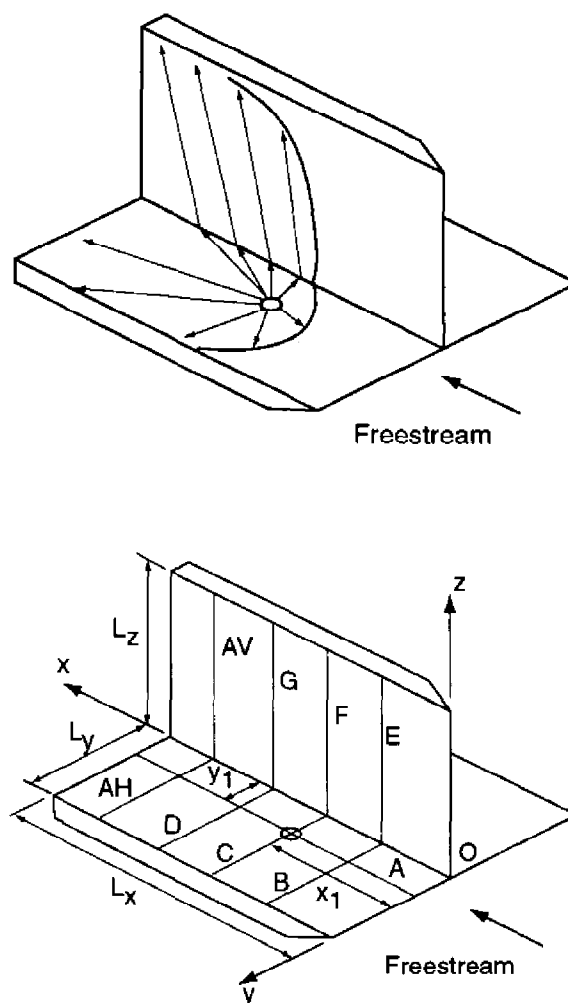

Fig. 1 Schematic of corner-flow/jet interaction test model.

sting radius was $R_b/4$ and the length was $6R_b$ or less since some of the test facilities were not able to accommodate stings of this length. Blunt body and rear sting dimensions are indicated in Fig. 2 where the base radius ranged from 2.5 to 76.2 mm.

2.2 Atmospheric Entry

The flight test cases consist of four individual cases to provide code-to-code comparisons for a 70° spherically blunted cone with a 2 m base diameter. No experimental results are available for these test cases. The test cases are for both Earth and Mars entry using both reacting and nonreacting gas models. The free-stream and surface boundary conditions are listed in Table 2. These conditions correspond to altitudes of approximately 85 and 68 km in the Earth and Mars atmospheres, respectively.

3-4

Table 1. Experimental test conditions

Test Case	T_0(K)	P_0(bars)	M_∞	Re_∞/cm	$\rho_\infty \times 10^5$ (kg/m³)	V_∞ (m/s)	T_∞(K)	λ_∞ (mm)	T_w (K)	Gas
(a) SR3 Wind Tunnel, CNRS Meudon; d = 5 cm										
1	1100	3.5	20.2	284	1.73	1503	13.3	0.671	300	N2
2	1100	10.0	20.0	835	5.19	1502	13.6	0.226	300	N2
3	1300	120.0	20.5	7253	46.62	1634	15.3	0.027	300	N2
(b) V2G Wind Tunnel, DLR Göttingen; d = 5, 2.5, and 0.5 cm										
1	575	2	15.6	719	6.70	1082	11.6	0.163	490	N2
2	675	5	16.5	1233	11.02	1173	12.2	0.103	565	N2
3	775	10	16.8	1935	17.25	1257	13.4	0.069	635	N2
(c) V3G Wind Tunnel, DLR Göttingen, d = 0.5 cm										
1	295	0.163	9.0	859	14.22	759	17.2	0.093	variable	N2
2	295	0.0549	9.0	286	4.74	759	17.2	0.278	variable	N2
3	295	0.0163	9.0	86	1.42	759	17.2	0.929	variable	N2
4	295	0.0054	9.0	29	0.47	759	17.2	2.808	variable	N2
(d) HEG, DLR Göttingen; d = 0.5 cm										
1	6713	576.0	10.1	7043	408.5	4539	489.9	0.017	300	Air
2	9244	385.0	9.5	2498	156.4	6075	856.4	0.044	300	Air
(e) LENS, Calspan Buffalo; d = 15.24 cm										
1	4351	74.1	15.6	578	13.06	3246	103.7	0.35	294	N2

Table 2. Flight test conditions[a]

Quantity	Earth Reentry	Mars Entry
Number density, m^{-3}	1.654×10^{20}	1.654×10^{20}
Temperature, K	180.65	141
Velocity, km/s	7.0	7.0
Mole fraction N_2	0.7628	0.05
Mole fraction O_2	0.2372	-----
Mole fraction CO_2	-----	0.95

[a] 70° blunted cone with base diameter of 2 m and a noncatalytic surface with a wall temperature of 1000 K.

θ = 70°

$R_n/R_b = 0.5$

$R_c/R_b = 0.05$

$R_j/R_b = 0.083$

$R_s/R_b = 0.25$

Rarefied Tests

CNRS Meudon, SR3
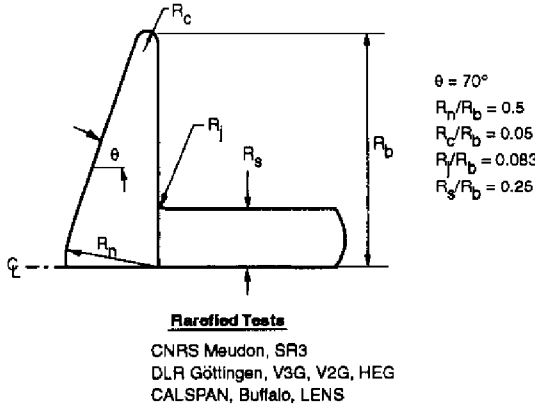DLR Göttingen, V3G, V2G, HEG
CALSPAN, Buffalo, LENS

Fig. 2 Blunt-body/wake-closure test model.

3 SCOPE OF EXPERIMENTS

3.1 Rarefaction

The manifestation of rarefaction is the existence of local nonequilibrium in the gas. This can be discussed by considering the scale length of flow gradients, L, where $L = |Q/\nabla Q|$ (where Q is any macroscopic flow parameter) and by comparing L with the mean distance traveled by molecules between successive collisions. In a subsonic flow, the molecular velocity is essentially the (randomly oriented) thermal velocity, and L is equal to the mean free path, λ. In a supersonic flow, the molecular velocity is essentially the (oriented) stream velocity $\vec{V}$, and L is equal to $\vec{V}/v$ where V is the collision frequency. In a subsonic flow, a local rarefaction parameter (or local Knudsen number) is defined as

$$\mathcal{P} = \lambda \times \left|\frac{\nabla Q}{Q}\right| \tag{1}$$

In a supersonic flow, the gradient must be projected on the direction of the flow and the rarefaction parameter is defined as

$$\mathcal{P} = \frac{1}{v} \times \left|\frac{\vec{V} \cdot \nabla Q}{Q}\right| = \frac{V}{v} \times \left|\frac{\vec{V} \cdot \nabla Q}{VQ}\right| = \frac{s\sqrt{\pi}}{2} \times \lambda \times \left|\frac{\vec{V} \cdot \nabla Q}{VQ}\right|$$
$$= M\sqrt{\frac{\gamma\pi}{8}} \times \lambda \times \left|\frac{\vec{V} \cdot \nabla Q}{VQ}\right| \tag{2}$$

where s is the molecular speed ratio and γ the specific heat ratio. $\mathcal{P}$ can be interpreted as $(1/v) \times |D\ln Q/Dt|$, a parameter that was first introduced by Bird[11]. Bird found a breakdown of translational equilibrium for $\mathcal{P} \approx 0.02$ when Q represents the density.

Some quantities require more collisions than others to reach equilibrium. The number of collisions required is usually

characterized by a collisional number Z that ranges from a few units (for translation and rotation) to a few thousands (for vibration and chemistry). Equilibrium requires that $\mathcal{P} \ll 1/Z_Q$, where Z_Q is relative to the process considered.

When the flow gradients are governed by the collisional process rather than by the geometry (e.g., in a shock wave, in a Knudsen layer, etc.), we have $\mathcal{P} \approx 1/Z_Q$, $\mathcal{P} \approx 1$ for the most rapidly changing parameter. The gradient scale length is then

$$L \approx \lambda \quad \text{or} \quad L \approx \lambda s \frac{\sqrt{\pi} \cos(\vec{V}, \nabla Q)}{2}, \tag{3}$$

whichever is larger.

Although they have usually less physical meaning, global rarefaction parameters can also be defined by regarding L as a characteristic length defined by the geometry and flow conditions in some location in the flow field (e.g., in the free stream). In a subsonic flow, $\mathcal{P}$ is the usual Knudsen number $Kn = \lambda/L$, while in a supersonic flow, the adequate parameter $\mathcal{P}$ is $s(\sqrt{\pi}/2) \times Kn \approx s \times Kn$. An estimation of the mean free path, λ, is given by Bird[12]

$$\lambda = \frac{\mu}{p\sqrt{2RT}} \times \frac{2(7-2\omega)(5-2\omega)}{15\sqrt{\pi}} \tag{4}$$

for a Variable Hard Sphere (VHS) gas characterized by a power-law viscosity-temperature relationship $\mu \propto T^\omega$. In practice, this expression can be used to calculate the mean free path for given flow conditions of an arbitrary gas by using "local VHS properties" $\omega = \omega_L = (d\mu/\mu) \times (T/dT)$. The mean free path of nitrogen has been plotted in Fig. 3 as a function of pressure and temperature in a wide range that covers the experiments reported in the present chapter. The viscosity used in Eq. 4 to generate the results in Fig. 3 was that given by Sutherland's expression for temperatures above 100 K and a linear $\mu(T)$ function below 100 K. Values at the lower free-stream temperatures common to the low density
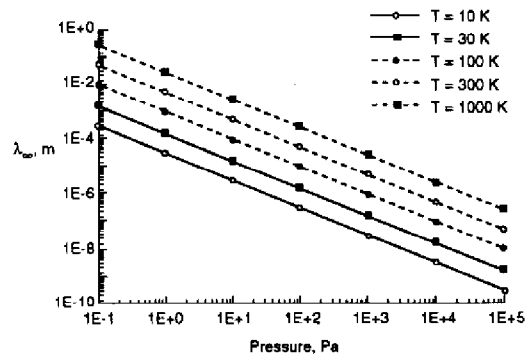

Fig. 3 Mean free path in nitrogen.

wind tunnel tests (Table 1) are problematic because of uncertainties associated with the low temperature gas properties.

3.2 Enthalpy

The experimental measurements for both test problems were made predominately at low enthalpy conditions, with free-stream enthalpy of the order of 1 MJ/kg. For these conditions, nonequilibrium effects are confined primarily to the translational and rotational modes. For the blunt body tests that were conducted in the impulse facilities, free-stream enthalpy was varied from 5 to 23 MJ/kg. These higher enthalpy conditions introduce additional complexities associated with vibrational and chemical nonequilibrium. The same is true of the two generic flight test conditions with enthalpy levels of approximately 25 MJ/kg.

4 CORNER-FLOW/JET INTERACTION RESULTS

4.1 Experiments and Results

Experiments were carried out at the Laboratoire d'Aérothermique du CNRS, Meudon, in facility SR3. They consisted essentially of wall pressure measurements. The experimental procedure and the results have been presented exhaustively by Allègre and Raffin[3]. Partial results have also been presented by Allègre and Raffin[2,4] and in the AGARD WG18 Phase I report[1].

4.1.1 Flow Conditions and Procedure

The experimental model consisted of two perpendicular flat plates oriented as shown in Fig. 1. Both plates were aligned parallel to the external flow direction. A hypersonic conical nozzle was embedded in the horizontal plate. The nozzle axis was vertical and the nozzle exit was flush with the plate surface. The nozzle was located at a distance $x_1 = 60$ mm downstream from the leading edge. Its geometry was characterized by throat and exit diameters of 0.213 and 1.53 mm, respectively, with a divergence half-angle of 9°.

The other plate was vertical, 60 mm high, and parallel to the external flow direction. Two configurations were investigated corresponding to the two distances y_1 of 15 mm and 30 mm between the nozzle and the vertical plate. The width L_y of the horizontal plate was equal to 40 and 55 mm in configurations 1 and 2, respectively. Both plates had sharp leading edges with bevel angles of 20°. The plates were equipped with 38 wall pressure orifices with diameters of 1 mm. Wall pressure distributions could be obtained along some arbitrary lines: $y = y_1$ on the horizontal plate (line A), and lines of constant abscissa x (B at $x = 40$ mm, C at $x = 60$ mm, D at $x = 80$ mm, AH at $x = 100$ mm on the horizontal plate and lines E, F, G, AV at the same values of x on the vertical plate). Lines A and C passed through the center of the exit section of the nozzle. The first measurements were obtained on a model 100 mm long and the other measurements on a model 120 mm long. The regions investigated on the two models overlap each

other and the pressures coincide within experimental uncertainty in the overlapping region.

The gas used for both the external free-stream flow and the jet was nitrogen. Three conditions for the free-stream flow could be realized (subscript ∞). The corresponding nominal values of the flow parameters are listed as part (a) of Table 1. Additional free-stream parameters are given in Table 3: pressure P_∞, stagnation pressure behind a normal shock P_{i2} and unit Reynolds number $Re_w = \rho_\infty V_\infty / \mu(Tw)$ based on viscosity at wall temperature $T_w = 300K$.

The nozzles used to generate the external free-stream flow had a conical divergent (continued by a cylindrical part for Conditions 1 and 2) and the free-stream flow was not uniform. Mach number distributions in the free-stream flow are given by Allègre[3] et al.

The jet flow was generated from a stagnation temperature of 300 K and stagnation pressures P_{0j} of 4, 12, and 20 bars. The nominal exit Mach number based on the nozzle geometry was 5.96. The jet flow rate $q_{m,j}$ and the jet exit conditions (subscript e) are given in Table 4. They have been obtained for a 1-D isentropic flow in the nozzle, coupled with a boundary layer.

The test matrix was obtained by combining

- the three external flow conditions (1,2,3 in part (a) of Table 1) and an additional case with the jet emerging into a quiescent atmosphere with no free-stream flow

- the two geometrical configurations ($y_1 = 15$ and 30 mm for Configurations 1 and 2, respectively)

- the three jet stagnation pressures $P_{0j} = 4, 12, 20$ bars and an additional case with the free-stream flow and no jet

The procedure used to measure wall pressures was as follows: the wind tunnel was started, and as soon as the stagnation conditions were correctly stabilized, the model was injected into the test section. This procedure reduced the risk of flow blockage by the model during wind tunnel startup. Furthermore, due to the time needed to measure the pressure, the wall-temperature rise was limited to 10–15 K. This rise made it unnecessary to water-cool the model, which facilitated the integration of the pressure tubes inside the

Table 3. Additional information for SR3 flow conditions

Condition	P_∞ [Pa]	P_{i2} [Pa]	Re_w [cm^{-1}]
1	0.0683	35.92	14.5
2	0.209	107.7	43.7
3	2.115	1145	427

Table 4. Jet exit conditions

P_{0j} [bars]	M_e	P_e [Pa]	T_e [K]	λ_e [mm]	q_{mj} [g/s]
4	5.288	544	45.5	5.3×10^{-4}	0.0327
12	5.532	1245	42.2	1.78×10^{-4}	0.0981
20	5.617	1893	41	1.07×10^{-4}	0.1635

model. A sting, rigidly attached to the rear portion of the model, provided the connection to a streamlined transverse support mechanism. This support was actuated by a pneumatic elevator to inject and retract the model in and out of the test section.

A pressure bench, including 5 Validyne DP 103 pressure transducers, was mounted inside the test chamber at a distance of approximately 400 mm from the model. The transducers have a high sensitivity and can measure pressures as low as 1 Pascal. A Turbovac 50 vacuum turbomolecular pump provided the vacuum (approximately 10^{-4} Pa) used as a reference pressure. Careful outgassing and calibration were made before each series of pressure measurements. Pressure distributions are presented by Allègre[3] et al. in tables and figures and are summarized hereafter.

4.1.2 Results

Experiments conducted in a background pressure P_∞ of about 2 Pa without external flow result in a moderate interaction of the jet with the walls: the wall-to-background pressure ratio varied from 0.69 to 1.19 and 0.50 to 1.44 in Configuration 1 for P_{0j} equal to 4 and 20 bars, respectively. There was less interaction with Configuration 2.

The pressure distribution along line A is plotted in Fig. 4 (part a) for Condition 1 and Configuration 1. When the jet is on, it acts as a barrier. When compared with the no-jet case, a substantial increase of the pressure on the horizontal plate is observed just ahead of the jet and a decrease is observed behind it. The increase is the largest for the largest flowrate of the jet. Similar results are found for Configuration 2. The same observations are made for Condition 2.

For Condition 3, there is only a small increase of pressure ahead of the jet (Fig. 4, part b) and an increase (rather than a decrease) behind it. The difference in behavior compared with Conditions 1 and 2 is best understood when considering the pressure distributions on the vertical plate. For Condition 1 (Fig. 5, part a), the jet is seen to bend downstream, but does not "touch" the horizontal wall. For Condition 3 (Fig. 5, part b), the jet central line is strongly
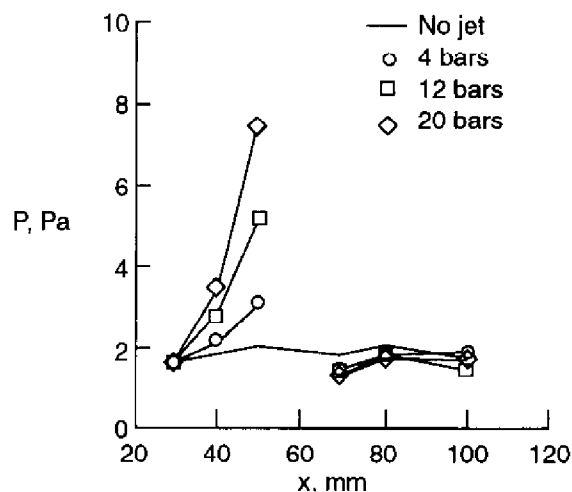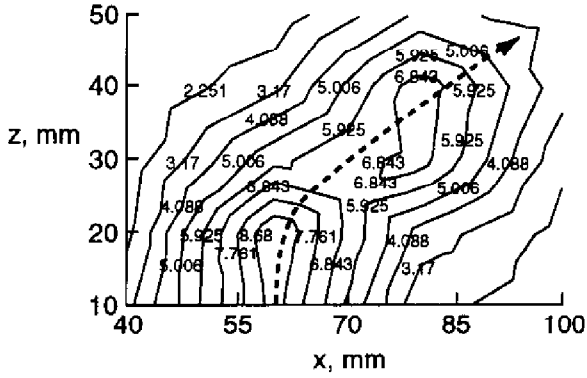

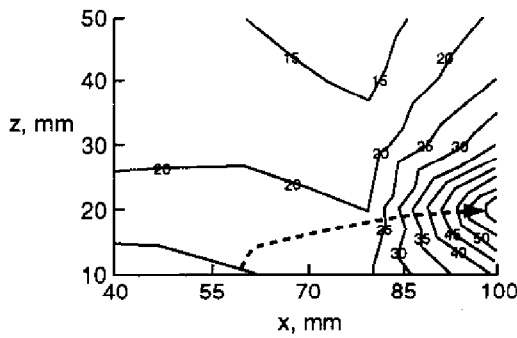(a) Test Condition 1.
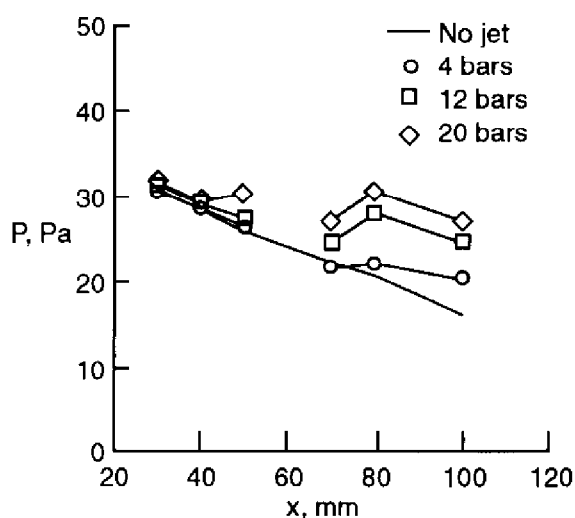
(b) Test Condition 3.

Fig. 4 Pressure distribution along line A in Configuration 1.

curved and the jet "touches" the horizontal wall, inducing a pressure increase.

Surface flow visualizations were obtained by oil-film deposit for Conditions 2 and 3 of the external flow and for the highest stagnation pressure of the jet (20 bars). The extent of the jet upstream influence on the wall flow is approximately the same when deduced from the pressure distribution and from the visualization.

(a) Test Condition 1, P_{0j} = 4 bars.

(b) Test Condition 3, P_{0j} = 20 bars.

Fig. 5 Pressure measurements along the vertical plate in Configuration 1.

4.2 Computations and Comparisons

Computations have been carried out at Aérospatiale, at NASA Langley, and at the Laboratoire d'Aérothermique du CNRS.

4.2.1 Aérospatiale

The numerical work done at Aérospatiale has been presented by Chauvot[5] et al. They considered Configuration 1 with stagnation pressure P_{0j} = 20 bars for the jet and Condition 1 for the external flow. They used a combined approach with a 3D Navier-Stokes (NS) solver (CEL3DNS) and a 3D DSMC code (JMC3D). The NS calculation included the converging part of the nozzle. It was first carried out in the jet region, with a limited extent into the external flow domain. The authors found that the calculated mass flow rate of the jet was 78% of the inviscid 1D estimation. They considered a boundary surface in the NS flow field and used the flow parameters on this surface to start a DSMC calculation beyond it. In a first simulation, the boundary surface was placed in the nozzle exit plane. In the final simulation, the NS calculation was extended by 20 mm into the dense part of the jet, and the DSMC calculation was extended 0.8 mm into the

nozzle in order to include the nozzle lip region. The DSMC mesh was refined near the plates and near the injection surface.

Both simulations give similar results. Good agreement was found between experimental and computed wall pressures without the jet. When the jet is on, the main features of the pressure distribution are found (Fig. 6) but the agreement is poor on the downstream part of the plates, where the pressure level is low.

In a previous calculation, a commercial code PHOENICS was used instead of the CEL3DNS code. An empirical adjustment, consisting of limiting the jet flow rate to 60% of its inviscid 1D value, was needed to provide the best agreement between numerical and experimental pressure distributions.

4.2.2 CNRS

Hendriadi[6] presents results obtained by DSMC calculations of Configuration 1 in Condition 1 (P_{0j} equal to 4 and 20 bars) and in Conditions 1 and 2 without the jet. He used the code DISIRAF, developed at the Laboratoire d'Aérothermique du
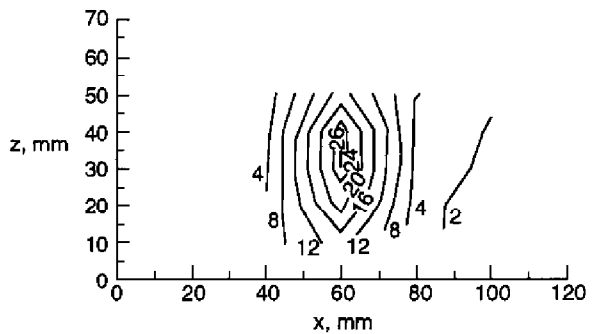
(a) Experiment.
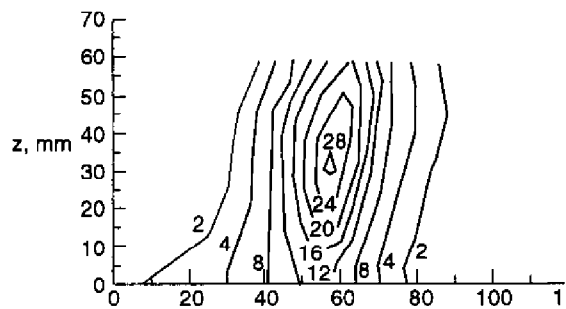
(b) Calculated, Chauvot et al.[5]

Fig. 6 Pressure measurements and calculations on vertical plate in Configuration 1, P_{0j} = 20 bars.

CNRS, with a rectangular 3D mesh refined near the walls and near the jet exit. The jet was generated by injecting the adequate flow rate of molecules through the horizontal wall, with distribution functions based on a 1D isentropic expansion from the stagnation conditions to the nozzle exit (uniform nominal exit conditions).

For Condition 1, good agreement is found between the experimental and calculated pressures when the jet is off. The agreement is worse for Condition 2. When the jet with $P_{0j}=20$ bars is on, the same observations as for Aérospatiale's calculations can be made. For the jet with $P_{0j}=4$ bars, the pressures calculated on the horizontal plate agree reasonably well with the experiment. However, the experimental jet appears to bend more strongly than the calculated one, which is clearly visible on the pressure distribution on the vertical plate.

4.2.3 NASA Langley

Tartabini[7] et al. (see also Tartabini[8] et al. for an early version of the paper) present results obtained by a 3D DSMC calculation for Configuration 1 in Condition 1 with a jet characterized by $P_{0j}=4$ bars. A no-jet case was also studied for comparison. It reveals a rather good agreement between computed and experimental pressure distributions. A correction for the orifice effect proposed by Potter and Blanchard[13] was applied to the experimental data, which improved the agreement. The jet was simulated by injecting molecules at the adequate location through the horizontal wall. The characteristics of the injection corresponded to the jet flow rate and to the velocity and temperature profiles in the exit plane of the nozzle, as calculated by a Navier-Stokes calculation of the nozzle flow using the VNAP2 code[14], with the calculation started at the nozzle throat. As for Hendriadi's corresponding calculation, the computed pressures exhibited similar trends to those indicated by the experimental measurements. However, quantitative agreement was not achieved over the whole surface of the plates.

Further calculations relative to the same problem have been carried out by Wilmoth and Tartabini[9]. They examined a number of potential reasons for the discrepancy between experimental and numerical results. By lowering artificially the stagnation pressure of the jet (2.4 bars in place of 4 bars), the jet plume shape was more consistent with the experiment, and gave the best agreement between experimental and calculated pressures. This behavior is consistent with the observation that was made by Chauvot[5] et al.

4.3 Discussion

Comparisons between experimental and calculated pressure distributions for the most rarefied external flow (Condition 1) are presented in Fig. 7 parts (a) and (b) for $P_{0j}=4$ and 20 bars, respectively.
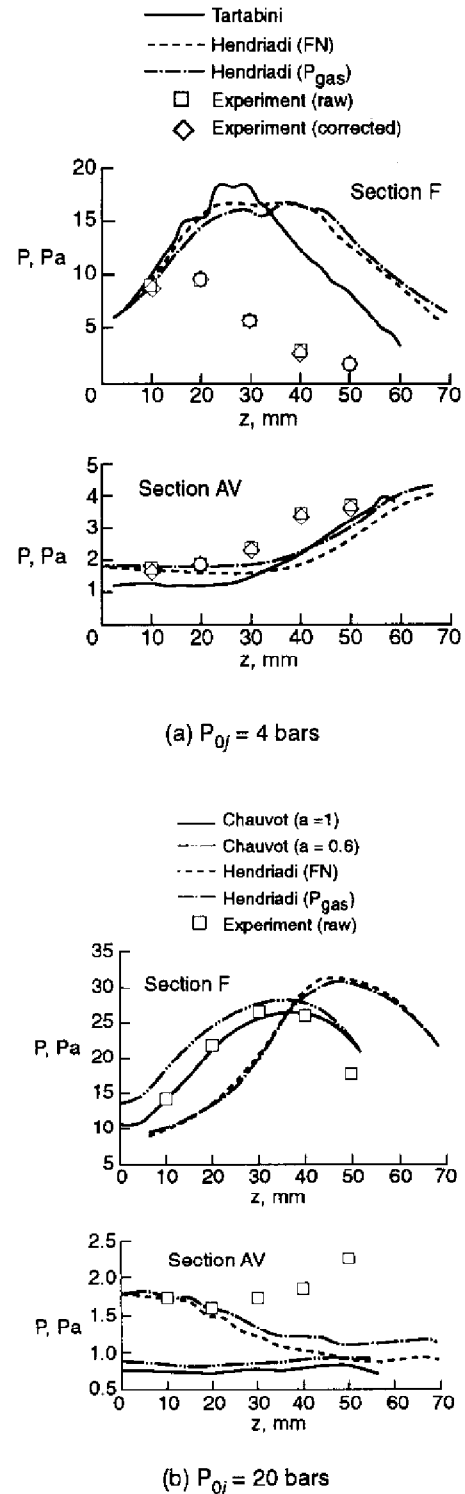

Fig. 7 Pressure profiles on vertical plate for Configuration 1 and test Condition 1.

All numerical calculations performed for the present problem are based on a continuum description of the nozzle flow together with a DSMC calculation of the external flow. They differ by details in their implementation. Although results do not coincide exactly with one another, they exhibit similar trends and the same qualitative discrepancies with the available experimental pressure distributions. Different issues will now be considered to understand these discrepancies.

4.3.1 Discretization in DSMC Calculations

Macroscopic quantities are obtained by averaging information sampled over a cell. Thus, the size of a cell in the direction of a unit vector $\vec{x}$, δx, must be such that $\left|\left(\delta \vec{x} \cdot \nabla Q\right)\right| << |Q|$ where Q is the most rapidly changing flow parameter. In the direction of the gradient, the condition becomes

$$\delta x << L = |Q/\nabla Q|. \tag{5}$$

This condition is the same as for any numerical method. If the gradient length scale L is governed by the collisional process, it results from Eq. 3 that the condition can be very severe

$$\delta x << \lambda \quad \text{or} \quad \delta x << \lambda \text{cos}\left(\vec{V}, \nabla Q\right) \tag{6}$$

whichever is larger. Furthermore, in a DSMC calculation the exact position of molecules within a cell is disregarded for the treatment of collisions. This simplification is valid when the above conditions are satisfied. Introducing subcells and forcing colliding molecules to be selected within the same subcell allows conditions 5 and 6 to be satisfied more "loosely".

For example, the numerical results obtained by Wilmoth and Tartabini[9] are not grid independent, but a parametric study indicates that a further refinement of the grid would not improve the agreement.

Decoupling the processes of moving and colliding molecules with time step δt requires that δt be much smaller than the mean collision time $1/\nu$ and the probability of a molecule colliding during δt is small:

$$\delta t \times \nu << 1. \tag{7}$$

If condition 7 is not satisfied, a bias is introduced when sampling the collision partners; and transport properties are not simulated properly, but conservation laws are still satisfied. As confirmed by Chauvot[5] et al., results are not affected by violating condition 7 in regions where the flow is little dependent on transport properties (inviscid flow regions).

In the extreme situation when $\nu \delta t >> 1$, molecules come to a local equilibrium in the cell before all collisions corresponding to δt take place. To save computing time, Lengrand[15] et al. proposed that computing collisions in a cell be stopped as soon as they do not change the distribution functions. The number of collisions allowed is set equal to some multiple of the number of molecules in the cell. Tartabini[7] et al. use the same technique in the central part of the jet.

Another condition on δt is due to the collisions being calculated at discrete times separated by δt rather than continuously. This condition requires that the variations of macroscopic flow parameters are negligibly small along the distance traveled by molecules during δt. In a locally supersonic flow, this condition is expressed as $\left|\delta t \times \left(\vec{V} \cdot \nabla Q\right)\right| << |Q|$. In a locally subsonic flow, it is expressed as $\delta t \times \vec{c'} << |Q/\nabla Q|$ or $\delta t \times v << |Q/\nabla Q|/\lambda$. If the local rarefaction parameter P is introduced, both conditions for supersonic and subsonic flows have the same expression

$$\delta t \times v \times P << 1. \tag{8}$$

In the dense part of the flow, P is very small and condition 8 is less severe than condition 7. It must be satisfied even if condition 7 is not. Otherwise flow gradients are "smeared" due to the numerical process.

Calculations where condition 7 is satisfied (Ref. 5 in simulation 1) and calculations where it is not satisfied (the other ones) result in similar discrepancies with the experiment. There is no indication that the discrepancies observed between numerical and experimental results are due mainly to time or space discretization.

4.3.2 Boundary Conditions

None of the calculations include iterative coupling between nozzle flow and corner flow. Rather, the conditions in (or near) the nozzle exit plane are estimated and taken as input boundary conditions for the DSMC calculation.

For the combination of the lowest P_{0j} with the less rarefied external flow, the jet emerges into the external flow with a pressure that is lower than the stagnation pressure P_{i2} behind a normal shock wave. Thus, it may not present the usual structure of an underexpanded jet. In all other cases, the jet is underexpanded. The nozzle lip exerts some upstream influence on a distance of a few local mean free paths and this affects the profiles of flow parameters near the lip. For a vacuum expansion, the external part of the jet (typically the backflow region) is also affected, and it is desirable to include

the nozzle lip in the DSMC computational domain. For the present problem, the jet expansion is limited by the external flow and the upstream influence of the nozzle lip can be disregarded. Chauvot[5] et al. found no difference when including it in the DSMC region.

The papers considered for this discussion do not include details on the flow conditions retained along the lateral, upper, and downstream boundaries for the calculations. If the subsonic (or low-supersonic) part of the corner downstream boundary fails to be reproduced, the pressure on a small region near the trailing edge is affected (it extends approximately 20 mm for Condition 1). The failure to reproduce the exact flow conditions along the upper boundary (through which the jet leaves the computational domain) may affect the bending of the jet and the pressure distribution along the vertical plate.

All calculations consider the free-stream conditions in the external flow to be uniform, whereas the actual experimental conditions are not uniform. However, this approximation has little consequence as indicated by the fact that the experimental and calculated pressure distributions are in good agreement when the jet is off.

4.3.3 Physical Modeling

The VHS model used in DSMC calculations cannot reproduce the real transport properties over the whole temperature range encountered. Results are nevertheless acceptable if they are reproduced correctly in regions where they actually govern the flow. This is the case in Tartabini's calculations where the simulated viscosity is correct at 300 K (near the wall), but high by a factor of 2 in the free stream.

The model used for rotational energy exchange also affects the pressure distribution. However, Wilmoth[9] et al. show that changing the model has only a moderate influence on the discrepancy between calculated and experimental results.

The model used for gas-surface interaction also affects the pressure distribution. Diffuse reflection with full accommodation is usually assumed in the calculations. Chauvot[5] et al. found no clear improvement of the calculation by reducing the accommodation from 1 to 0.6.

A potential problem is due to condensation occurring during the experiment, but it is not taken into account in the calculations. A part of the flow field is well within the liquid domain of a (P,T) diagram. When designing the SR3 facility, the absence of condensation in the free stream was checked. However, condensation remains possible in the jet.

4.3.4 Experimental Uncertainty

The accuracy of pressure measurements at pressures as low as 1-2 Pa is poor. In particular, the pressure measured is affected by the temperature of the wall. However, this uncertainty is not sufficient to explain the discrepancies observed at higher pressures.

A more serious cause of experimental error is due to the small size of the nozzle. Any error on its dimensions would affect the flow rate and the exit conditions of the jet, and thus its interaction with the external flow.

The mean free path at $T_w = 300$ K ranges from 5.5 mm to 0.08 mm when the pressure ranges from 1 to 70 Pa. The pressure taps have a diameter of 1mm. Thus, the question of the orifice effect on pressure measurements must be considered. This effect is hardly an experimental uncertainty, but rather a real difference between two physically distinct quantities. On one hand the "calculated wall pressure" is the normal stress due to the exchange of normal momentum of molecules striking the wall. Hendriadi[6] shows that there may be a large difference between this quantity and the thermodynamic pressure of the gas at the wall (deduced from the equation of $P = nkT_{tr}$, with number density n, Boltzmann constant k, and translational temperature T_{tr}). This difference is an indication of nonequilibrium. On the other hand, the "experimental pressure" is the equilibrium pressure in a transducer cavity connected to the pressure tap. Previous experience indicates that the experimental pressure is much closer to the normal stress than to the thermodynamic pressure of the gas close to the wall. However, there is no simple relation between them. Orifice corrections (as that applied by Tartabini et al. to the experimental pressure) are attempts to make them coincide, but they cannot be claimed to apply to situations other than those that where used to establish them. However, as can be seen in Fig. 7, discrepancies between experimental and calculated pressures occur even under conditions where nonequilibrium and orifice corrections are small.

5   BLUNT-BODY/WAKE-CLOSURE RESULTS

Experiments and computations have been performed for the same forebody configuration: a 70° spherically blunted cone with a nose radius equal to one-half the base radius and the corner or shoulder radius equal to 5 percent of the base radius (Fig. 2). Computations have been made for both wind tunnel and generic flight conditions for the same forebody configuration. Results of experiments performed in each of five hypersonic test facilities are briefly summarized along with some of the findings of the computational studies that have been made for specific test conditions.

The nominal test conditions for the low density wind tunnels participating in the AGARD WG 18 investigation are listed in Table 1. Also included are the test conditions for two impulse facilities that were used to achieve rarefied flow. One test was run in the Large Energy National Shock Tunnel (LENS) facility[16-17] at a low pressure condition to produce Mach 15.6 nitrogen flow. Also, tests[18] were conducted at the highest
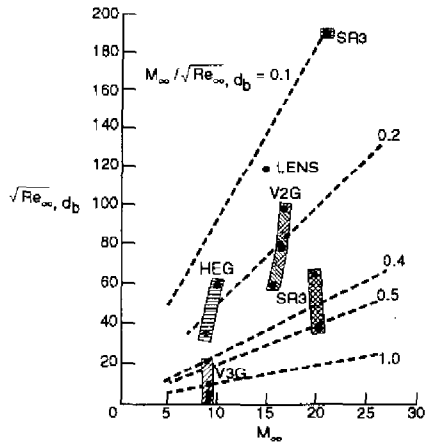
Fig. 8 Experimental test conditions in terms of the rarefaction parameter $M_\infty/\sqrt{Re_\infty}$.

enthalpy conditions in the HEG (High Enthalpy Göttingen) free piston shock-tunnel using very small models ($d_b = 5$ mm). Two of the HEG test conditions are included in Table 1. Fig. 8 displays these test conditions in terms of rarefaction, as indicated by lines of constant $M_\infty/\sqrt{Re_\infty}$, where the characteristic dimension is the base diameter. The larger this parameter is, the greater the flow rarefaction.

These test conditions provide a range of flow environments that include both nonreacting and reacting flows. Also, thermal nonequilibrium issues exist for even the lowest enthalpy tests (translational, rotational, etc.) with more internal modes participating for the higher enthalpy flows.

Hence, the conditions include a variety of flow environments that serve as test cases to measure the ability of computational codes to calculate such flows where compression, expansion, and separation are key features. Table 5 lists the organizations that have made one or more computations for the experiments and generic flight test conditions. The significant number of DSMC codes applied to this activity are representative of current capabilities both in terms of solution algorithms and physical modeling. The two Navier-Stokes codes are the Langley aerothermodynamic upwind relaxation algorithm (LAURA) of Gnoffo[19-20] and a code developed at North Carolina State University by Olynick[21-22] et al.

5.1 CNRS Tests (SR3)

Allègre [23-24] et al. provide detailed information concerning the experiments conducted by the CNRS at Meudon, France, using the SR3 wind tunnel. The test matrix included three free stream flow conditions (Table 1), the same conditions as for the corner-flow/jet interaction experiments. The free-stream was nitrogen at a nominal Mach number of 20 and Reynolds number, based on model base diameter, ranging from 1,420 to 36,265. Measurements were performed that obtained three sets of data: density flow fields, heating rate

distributions, and aerodynamic forces and moments. Density flow-field measurements were made with the electron beam fluorescence technique for the two more rarefied conditions and for two angles of incidence: 0° and 10°. Heating rate distributions along the forebody, base, and sting, as well as aerodynamic forces, were obtained for angles of incidence between 0° and 30°.

5.1.1 Procedures and Representative Results

Three different models were used according to the type of measurement, each having a 5 cm base diameter and an afterbody sting. For aerodynamic force measurements, the model was made of aluminum and uncooled. The model was directly attached to an external balance mounted around the open-jet test section of the SR3 wind tunnel. The model used for the flow-field density measurements was made of brass, water cooled, and sting supported. For heat-flux measurements, a thin-wall model made of Armco steel elements was used (Fig. 9). Chromel alumel thermocouples were embedded through the wall thickness at nine locations along the forebody, base plane and sting ($s/R_n = 0.00$, 0.52, 1.04, 1.56, 2.68, 3.32, 5.06, 6.50, and 7.94). Additional details concerning the models, test procedures, and tabulated and graphical presentations of results are documented by Allegre and Bisch[23]. Examples of data obtained for heat transfer and aerodynamics are presented in Figs. 10 and 11, respectively. The heating rate distributions as a function of angle of incidence are those for test Condition 2 (Table 1) while the axial (C_A) and normal (C_N) force coefficients are those for each of the three test Conditions as a function of incidence. Examples of the flow-field density measurements are discussed later.

5.1.2 Computations and Comparisons

Extensive computations have been made for the SR3 test conditions since the test parameters were defined well in advance of the actual experiments. Test Condition 2 (Table 1) was a test case of the 4th European High-Velocity Database Workshop, ESTEC, Noordwijik, The Netherlands, Nov. 1994. Eight DSMC solutions were presented at this workshop, and a summary of those results is given by Coron and Harvey[25].
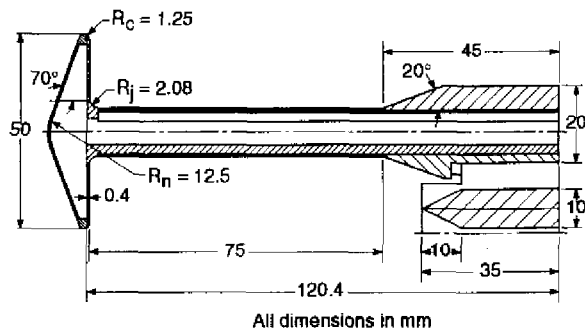

Fig. 9 Model for heat transfer rate measurements in SR3.

Table 5. Computational contributions for blunt-body/wake experimental and generic flight test conditions using direct simulation Monte Carlo (DSMC) and Navier-Stokes (NS) Codes.

| Contributors	Low Density Wind Tunnels			Impulse Facilities		Flight	
	SR3	V3G	V2G	HEG	LENS	Earth	Mars
Aerospatiale les Mureaux, France	DSMC[a]						
CNRS Meudon, France	DSMC						
Cornell University, U.S.A.	DSMC				DSMC		
DLR Göttingen, Germany	DSMC		DSMC				
DRA Farnborough, U.K.	DSMC						
Fluid Gravity, Hampshire, U.K.	DSMC						
Imperial College, U.K.	DSMC	DSMC			DSMC	DSMC	DSMC
ITAM, Novosibrisk, Russia	DSMC						
Middle East Tech. Univ., Turkey	DSMC					DSMC[a]	
NASA Langley, U.S.A.	DSMC[a] & NS		DSMC	DSMC	DSMC	DSMC	DSMC
North Carolina State University, U.S.A	DSMC[a] & NS				NS	NS	
Sandia Albuquerque, U.S.A.	DSMC						

[a]3-D solutions included
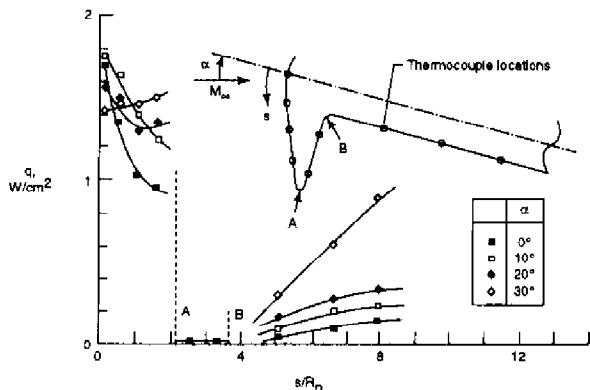
Fig. 10 Measured[23] heating rate distributions for SR3 test Condition 2.
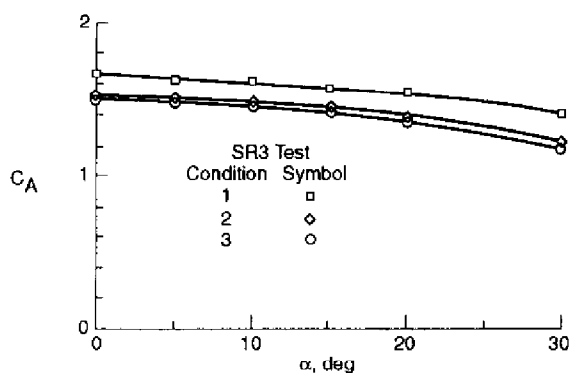
(a) Axial force coefficient.
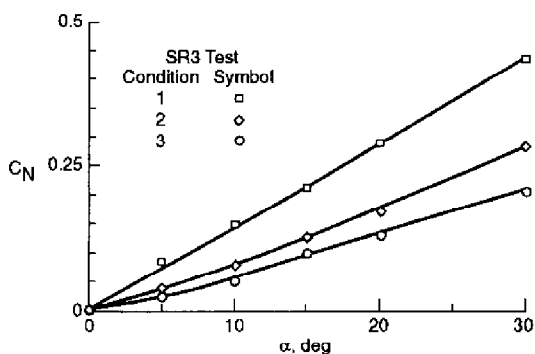
(b) Normal force coefficient.

Fig.11 Measured[23] aerodynamic coefficients for the three SR3 test conditions.

Calculations using both DSMC and Navier-Stokes solvers were made either prior to the experiments (Refs. 25 through 31, for example) or prior to release of the experimental data at the ESTEC Workshop. Moss[31] et al. provide an extensive presentation of information concerning flow-field features and surface quantities (including tabulated surface results) resulting from one set of DSMC calculations. Also reported in Ref. 31 are the results of parametric studies concerning numerics (cell size and time step) and physical modeling (rotational collision number and surface reflection model). Gilmore[29] also examined the effect of varying the surface accommodation coefficient from 0.5 (50 percent specular) to 1.0 (fully diffuse).

Examples of the calculated and measured results for the SR3 tests are shown in Figs. 12-14. Surface heating distributions at zero incidence are presented in Fig. 12 for each of the three test conditions. As evident by the comparisons, the DSMC solutions[32] show a better agreement with the measured values than do the Navier-Stokes[19-22] methods (with surface slip and temperature jump boundary conditions) along the base plane and sting, regions where rarefaction effects are most significant. The agreement of DSMC predictions and measurements is quite good along the sting and also on the base plane, where measured signal levels for Conditions 1 and 2 were so small that the heating magnitude could only be characterized as being less than 0.002 and 0.004 W/cm² for Conditions 1 and 2, respectively (indicated by symbol with downward pointing arrows in Fig.12).

Along the forebody, the agreement between calculated and measured results is not as good as expected[32]. Along the blunted cone forebody, agreement between calculation and measurement decreases with decreasing rarefaction. This is most evident for Condition 3 where the experimental value at $s/R_n = 1.56$ is 55 percent of the DSMC value. When the DSMC results along the forebody are compared with the Navier-Stokes solutions[32], the agreement is 10 percent or better. Currently, the discrepancy observed in measured and computed heat transfer distributions along the forebody remain unresolved. Further experiments should be conducted to resolve this issue.

Figure 13 presents the measured and calculated heat transfer distributions for Condition 2 with the model at incident angles of 0°, 10°, and 20°. The data are presented in terms of the heat transfer coefficient defined as $C_H = 2q/\rho_\infty V_\infty^3$. The calculated values for both the windward and leeward rays are the 3-D DSMC solutions of Pallegoix[30]. Heat transfer measurements were made only along the windward ray, and agreement between measurements and calculations is very good. Also, Nance[33] et al. obtained fair agreement with the experimental heat transfer measurements for Condition 1 at 10° incidence using two different 3-D DSMC codes, one using a uniform Cartesian gird and one an unstructured tetrahedral grid.
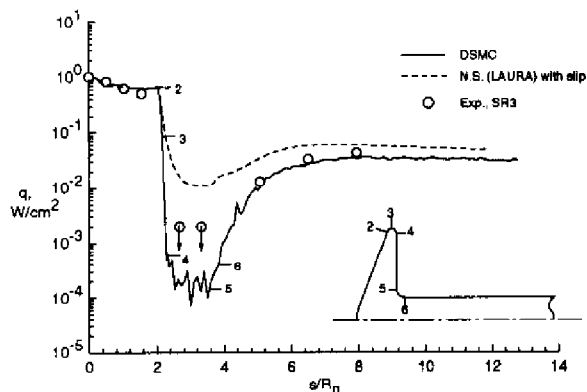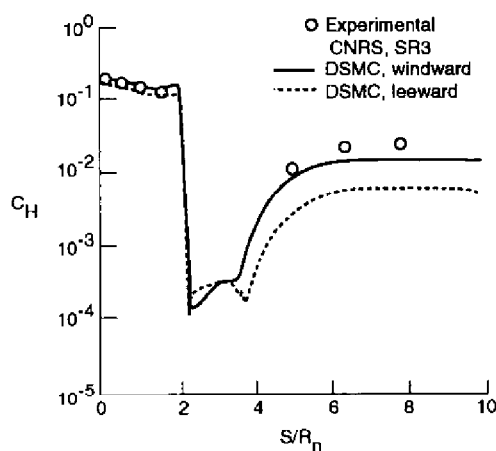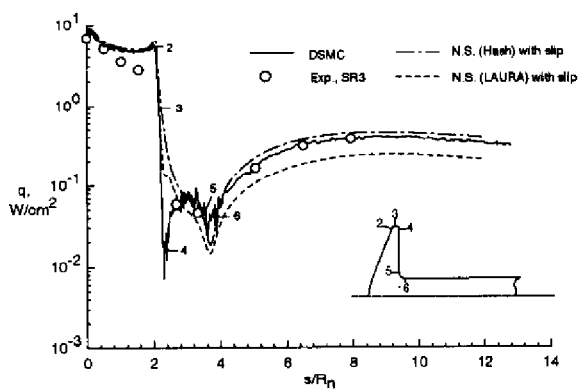
(a) Condition 1.
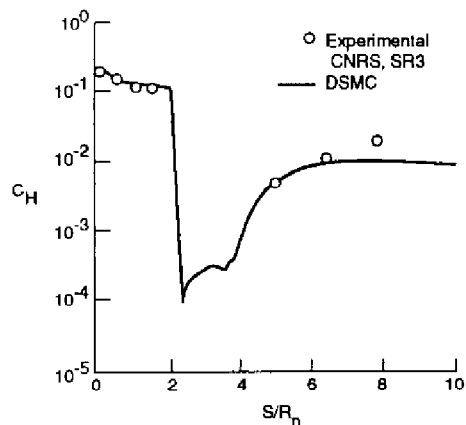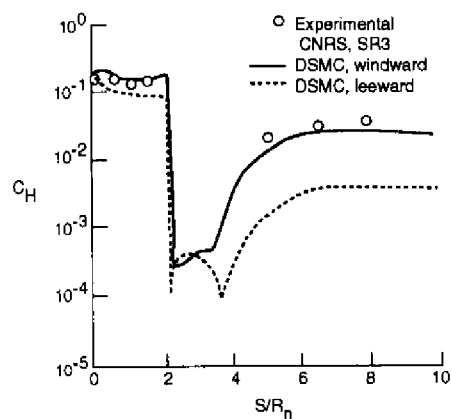

(a) Incidence = 0°.
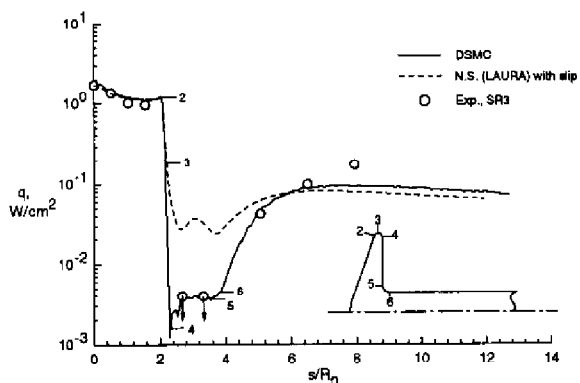
(b) Condition 2.

(b) Incidence = 10°.

(c) Condition 3.

(c) Incidence = 20°.

Fig. 12 Comparison of SR3 experimental[23] and computed[32] heating rate results (d = 5.0 cm).

Fig. 13 Comparison of SR3 experimental[23] and computed[30] heating rate distributions for Condition 2.
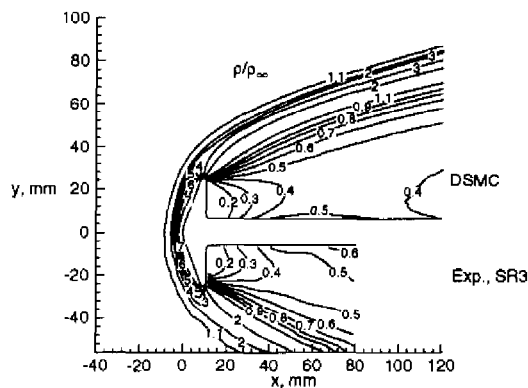
Fig.14 Comparison of measured[23] and calculated[32] density for SR3 test Condition 2.

A number of computational studies have presented graphical results of the forebody and wake flow features, demonstrating the influence of rarefaction on the flow structure. The DSMC calculations of Refs. 26 and 31 yield a wake vortex for each of the three test conditions with the size of the vortex increasing with decreasing rarefaction. Also, the location of maximum heating along the sting is downstream of the location of the free shear layer reattachment, as indicated by the sting shear stress distribution.

Wilmoth[27] et al. computed the flow for the SR3 test conditions without an afterbody sting using both DSMC and Navier-Stokes codes. These computations indicate that a wake vortex does not exist for Condition 1 but is present for the other two conditions, consistent with the finding of an earlier study of Dogra[34] et al. Wilmoth also demonstrated that a zonally decoupled DSMC solution procedure can be used effectively for these flow conditions (Kn_∞ ranging from 0.01 to 0.0005). That is, the forebody flow is solved separately by using either a DSMC or Navier-Stokes method, and the forebody exit-plane solution is specified as the in-flow condition to the decoupled DSMC solution of the wake region. The zonally decoupled solutions show good agreement with fully coupled DSMC solutions of the wake flow densities and velocities. The combined use of Navier-Stokes for the forebody with a decoupled DSMC solution for the wake provides an efficient method for solving transitional blunt-body flows where the forebody flow is continuum and the wake is rarefied. This approach has been employed in several studies[17,35-37] for much smaller Knudsen number cases than considered herein. The study of Hash and Hassan[37] concluded that the decoupled approach was more advantageous when applied to a small Knudsen number ($Kn_\infty \approx 10^{-4}$) problem than a hybrid coupled DSMC/Navier-Stokes solver.

As mentioned earlier, nonintrusive electron beam fluorescence measurements of flow-field density were

made[23], and Fig. 14 presents, as an example, a comparison of a DSMC calculation[32] with measured values. (See Ref. 25 for even better agreement of computed and measured results and Ref. 30 for good comparisons at 10° incidence.) The measured results are presented as the ratio of local density with the model installed in the test section of the wind tunnel to free-stream values without the model in the test section since density gradients exist in the undisturbed flow. The calculated results are local values ratioed to the free-stream value (Table 1). The overall quantitative features of the two data sets are similar, with the exception of the expansion of the flow about the outer corner of the model and the sudden up-turn of the 0.5 density contour adjacent to the sting. The calculated density contours in the near wake show a concentrated expansion from the rewarded facing portion of the outer corner. This behavior is consistent with other DSMC calculations that have been made for Condition 2, as summarized in Ref. 25, both at 0° and 10° incidence. The measurements show a more diffuse expansion extending down the base of the model. Part of this discrepancy may be due to a measurement resolution issue, since the gradients in density are substantial near the surface and occur in a rather small volume. As suggested in Ref. 25, the up-turn of the measured density contours along the sting are most likely due to an increase in the cross-sectional area of the sting starting 80.4 mm downstream of the forebody stagnation point of the model. The change in the sting configuration was not included in the numerical simulations.

The aerodynamic forces, moments, and center of pressure were also measured for each flow condition at six angles of incidence spanning 0° to 30°. Tabulated results of these measurements are presented in Ref. 23. As reported in Ref. 32, the maximum difference in the measured and DSMC calculated drag coefficients for zero incidence was 6 percent. Reference 30 presents DSMC results for axial, normal, pitching moment, and center of pressure results for test Condition 2 at 0°, 10°, and 20° incidence. The discrepancies with measured values are 11 percent or less.

5.2 DLR Tests (V3G, V2G, and HEG)

Blunted cone models with base diameters of 5, 25, and 50 mm were utilized in the DLR Göttingen tests exploring the effects of rarefaction on forebody and wake flows. Three different test facilities were used: the two vacuum wind tunnels V3G and V2G, and the high enthalpy facility HEG. A brief summary of the experiments performed and computations for selected tests follows.

5.2.1 V3G Tests and Computations

The experimental measurements made by Legge[18,38] with the V3G free-jet facility concentrated on aerodynamic and heating measurements to provide data for validating theoretical results. The model was a 5 mm base diameter copper model suspended by means of 0.06 mm diameter thermocouple leads. Drag, lift, global aerodynamic heat transfer, and recovery temperature were measured in a Mach 9 nitrogen free-jet flow. These measurements were made at

stagnation temperatures of 300 K and 500 K for various degrees of rarefaction. The wall-to-stagnation temperature ratio was varied between 0.8 and 1.5. The desired wall temperature is established and maintained at a constant value before the flow is started by means of two radiators (Fig. 15). The global aerodynamic heat transfer rate to the blunted cone model was determined by using the model itself (Fig. 16) as a calorimeter. Lift and drag were determined by means of an electromagnetic two-component balance. Angle of attack results were obtained for $\alpha = 0°$, 20°, and 40°. The estimated overall errors for the measurements were ± 8% at $T_0 = 300$ K and ± 12% at $T_0 = 500$ K. Additional details concerning the experiments, data reduction, data accuracy, and results are included in Refs. 18 and 38.

The drag coefficient (Fig. 17), along with the other force coefficients, have the usual behavior between continuum and free-molecular flow. That is, there is a smooth transition between the continuum and free-molecular values for complete accommodation. The aerodynamic curves for $T_0 = 300$ K and 500 K agree well, which means that the Knudsen number, $Kn_0 = 3.2\mu_0 / \left(\rho_\infty \sqrt{2\pi R T_0} \cdot d_b \right)$ is a reasonable correlation parameter when T_0 is changed. This behavior is demonstrated in Fig. 17 where the drag coefficient is plotted for $T_0 = 300$ K and $T_0 = 500K$ at $T_w/T_0 = 1$. For $\alpha = 0$, $T_0 = 1100$ K and $T_w = 300$ K, two numerical results (Dogra[34] et al.) are also included: (1) $M_\infty = 20.2$, $\rho_\infty = 1.73 \times 10^{-5} kg/m^3$, $C_D = 1.61$, $Kn_0 = 0.11$ and (2) $M_\infty = 19.7$, $\rho_\infty = 5.19 \times 10^{-5}$ kg/m³, $C_D = 1.54$ and $Kn_0 = 0.038$. The smooth transition from continuum to free-molecular values was not observed for the heat transfer and recovery temperature data at the higher wall-to-total temperature ratios. The heat transfer coefficient, $C_H' = 2\dot{Q} / \left(\rho_\infty U_\infty^3 A \cos \alpha \right)$ where $\dot{Q}$ is the global heat transfer rate and the cone reference area is $A = \pi R_b^2$ follows the same
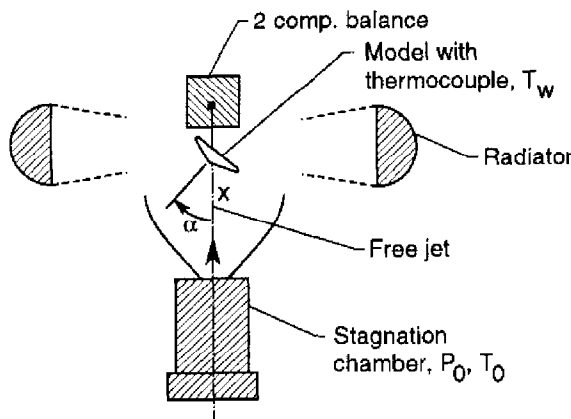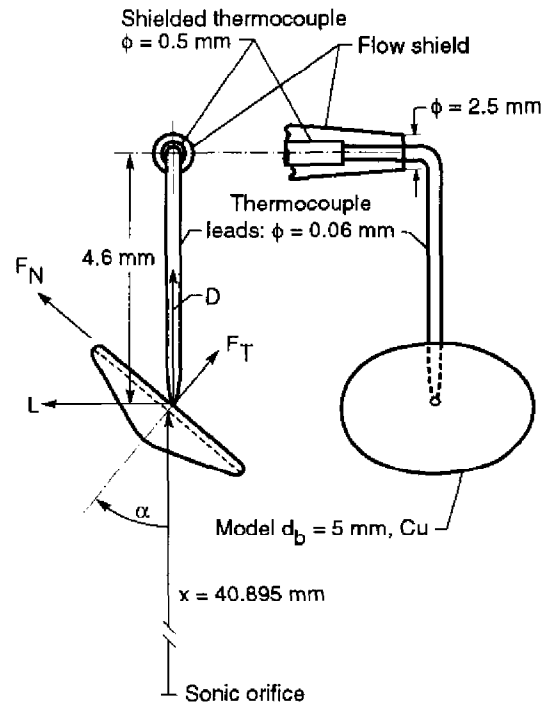

Fig. 16 Suspension of cone model and coordinate system for global heat-transfer rate and force measurements in V3G.

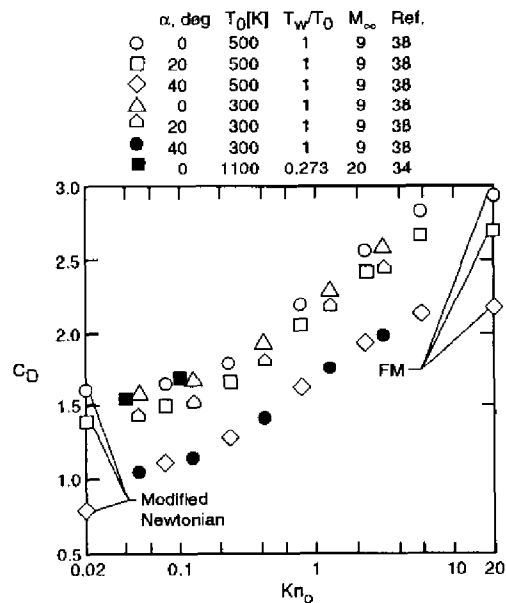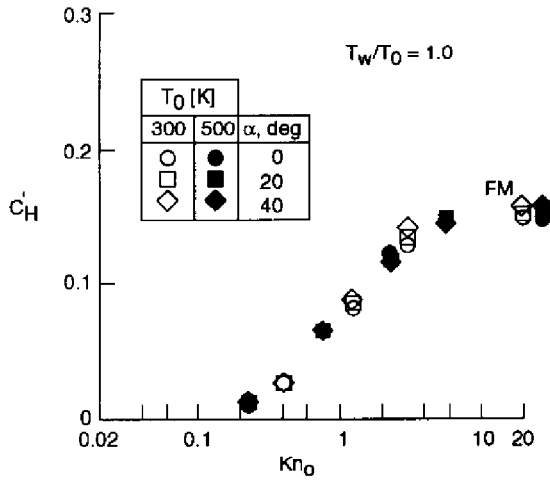| α, deg	T₀[K]	T_w/T₀	M∞	Ref.
○ 0	500	1	9	38
◻ 20	500	1	9	38
◇ 40	500	1	9	38
△ 0	300	1	9	38
◓ 20	300	1	9	38
● 40	300	1	9	38
■ 0	1100	0.273	20	34

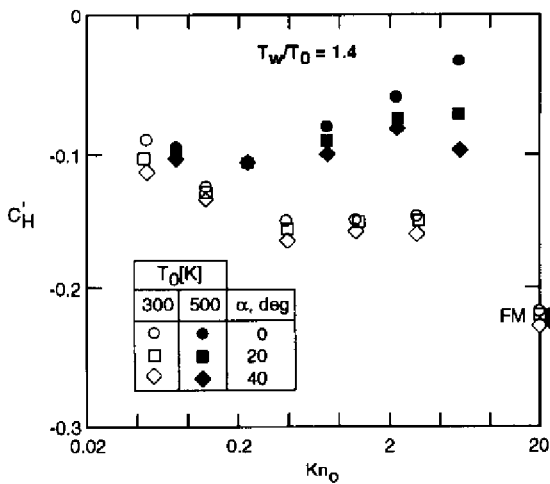

Fig. 17 Drag coefficient as a function of Kn_0 and comparison of DSMC and experimental results for different flow conditions (V3G).

Fig. 15 Schematic of experimental set-up for V3G Göttingen blunted-cone tests.

(a) $T_w/T_0 = 1.0$.

(b) $T_w/T_o = 1.4$.

Fig. 18 Heat transfer coefficients C'_H (based on $A' = A \cos \alpha$) as a function of Kn_0 (V3G).

curves for both $T_0 = 300$ K and $T_0 = 500$ K at $T_w/T_0 = 1.0$ as shown in Fig. 18(a). At larger T_w/T_0 values; however, the absolute value of C'_H becomes smaller for $T_0 = 500$ K than $T_0 = 300$ K, indicating that the accommodation coefficients becomes less with increasing T_w. This behavior is demonstrated in Fig. 18(b) where C'_H is plotted as a function of Kn_0 and $T_w/T_0 = 1.4$ for the two total temperature conditions and three angles of attack.

DSMC calculations have been made by Gallis and Harvey[39-40] for the zero incidence test conditions at $T_w/T_0 = 1.0$ for both $T_0 = 300$ K and 500 K. The DSMC

simulation modeled collisions with the variable soft sphere collision model[41] and energy exchange with the Maximum Entropy model[40]. The surface was assumed to be diffusely reflecting with full accommodation. The computational and experimental results are in good agreement for almost all cases simulated as demonstrated in Figs. 19(a) and 19(b) for the $T_0 = 300$ K results where the drag and global heat transfer coefficient $\left(\overline{C}_H = 2\dot{Q}/\rho_\infty V_\infty^3 A\right)$ results are presented, respectively. The good agreement between V3G experimental measurements and DSMC calculations has also been evident for other configurations as discussed in Ref. 42 for a disk and in Ref. 43 for a delta wing.

5.2.2 V2G Tests and Computations

The vacuum wind tunnel V2G at DLR, Göttingen, has been used extensively to support the blunt body/wake research. Both qualitative and quantitative data have been reported by Legge[18,44,45] for models with and without a sting. The experiments were conducted in rarefied nitrogen flow at a nominal Mach number of 16 (see Table 1). Calibration results for the 15° half angle conical nozzle used to produce the flow is reported in Ref. 46. Reference 44 details many of the
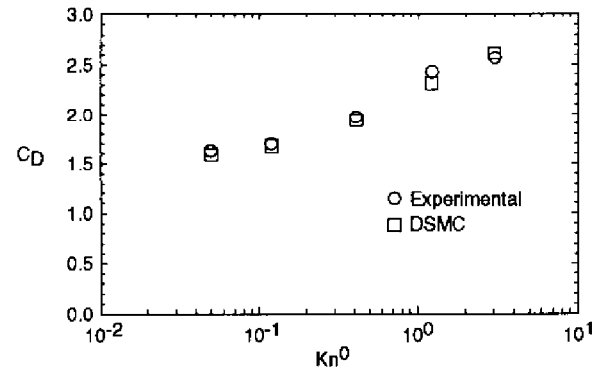
(a) Drag coefficient.
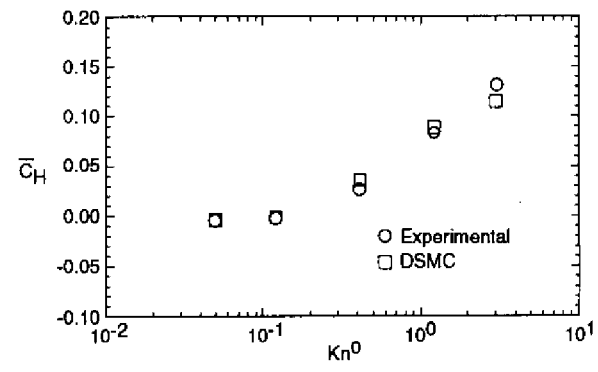
(b) Global heat transfer coefficient.

Fig.19 Comparison of V3G experimental[38] and DSMC[39] results for blunted at zero incidence.

qualitative results obtained for 50 and 25 mm base diameter models with and without (wire suspension) stings. The data include high frequency glow discharge flow visualization showing the shock shape, oil flow pictures giving surface streamlines, liquid crystal surface temperature visualization providing lines of constant temperature (lines of constant heat transfer under certain restrictions), and pitot pressure measurements in the wake. Data obtained with a 5 mm base diameter model is included in Ref. 18.

DSMC computations by both Danckert[47] and Moss (Appendix A of Ref. 45) were made for the V2G test conditions (Table 1) for the test model without a sting. Both DSMC codes are based on the method of Bird[11]. Comparisons of the V2G measurements with the DSMC results are presented in Ref. 18 where it is stated that excellent agreement is achieved between the calculated and experimental shock shapes (deduced from glow discharge visualization). The experimental shape for the 10 bar condition runs between the calculated iso-density lines (value normalized by free-stream density) of 2 and 3. For the same test condition, it was shown in Ref. 18, that the heating distribution along the sting, inferred from the liquid crystal heat transfer visualization measurements, was in reasonable agreement with the DSMC calculations. As discussed in Ref. 18, the data extraction process used the DSMC heating results at an arbitrary location to infer the quantitative values at other locations along the sting.

Global heat transfer and recovery temperature measurements were also made in V2G by using a 5 mm base diameter model. When the recovery temperature and Stanton number (Fig. 20)

$$St = \frac{\dot{Q}}{\rho_\infty U_\infty C_p (T_r - T_w) A}$$ (9)

results from V2G and V3G are compared, the agreement is generally good. This agreement confirms[18] that Kn_0 is a good
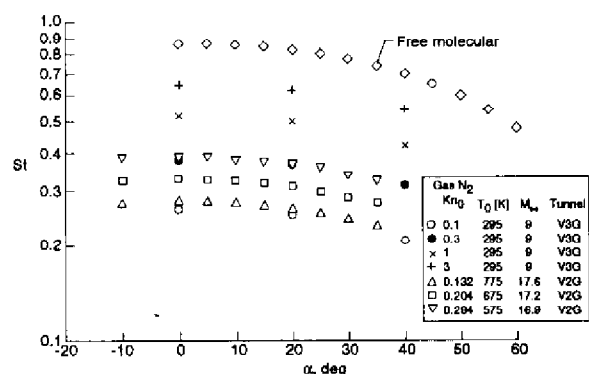
correlation parameter in the rarefied regime for wind tunnels with $T_0 < 2000$ K. These data also confirm that good agreement can be achieved between free jet data (V3G) and conical nozzle data (V2G) which has much smaller gradients, provided the reference point for the free-stream conditions is addressed[18] for the free jet flow.

In addition to the wake density measurements made in the SR3 wind tunnel of CNRS, a study was conducted on the wake flow features under rarefied hypersonic flow conditions using the Göttingen V2G wind tunnel. The establishment of a vortex in a highly nonequilibrium flow (non-Maxwellian distribution function of the translational degrees of freedom) was investigated numerically with the DSMC[47] method and experimentally[45] with Patterson probe measurements. This intrusive measurement technique provides detailed information on the molecular number fluxes, hence information on the wake vortex features and how it is influenced by rarefaction.

Details of the experimental setup and flow conditions (three conditions listed in Table 1 for V2G), along with the theoretical aspects of the Patterson probe measurements, are given in Ref. 45. The measurements were made behind a blunted cone model (without sting) with a base diameter of 50 mm while suspended by three thin tungsten wires fixed at the backside. The coordinate system and the Patterson probe geometry are given in Fig. 21, where x is the distance on the wake centerline from the model nose. The Patterson probe could be moved in x- and y-directions and could be turned 360 deg around the slit (not the probe axis), where the slit center was located at $z_p = 0$.

Fig. 20 Global Stanton number as a function of angle of attack and Knudsen number as measured[18] in V3G and V2G.
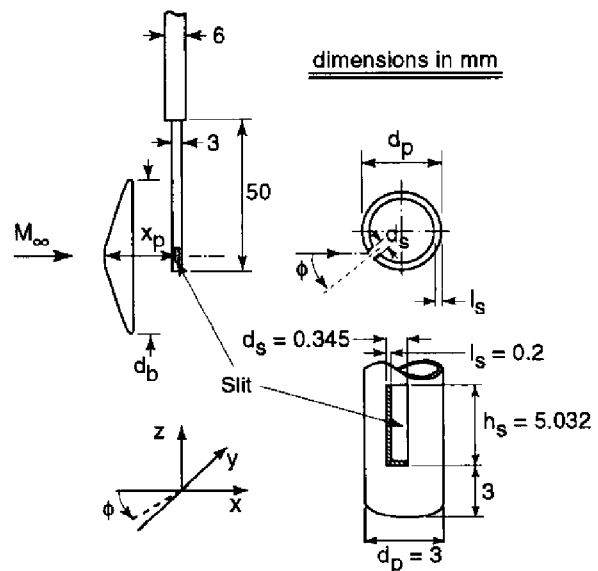

Fig. 21 Model and Patterson probe geometry used in V2G experiments ($d_b = 50$ mm).

An example of the experimental and numerical results for test Condition 1 (p_0 = 2 bar) is presented in Fig. 22. Shown is the incoming number flux, $\dot{n}_i$, at the entrance plane of the Patterson probe slit normalized by the free-stream mass flux as a function of the probe turning angle ϕ (for ϕ = 0°, the slit is facing the negative x-direction) for various probe locations, x_p, measured downstream of the cone nose. The value of x at the cone base plane was 10.4 mm. At x_p = 15 mm, the existence of a vortex is indicated by the fact that $\dot{n}_i$ (ϕ = 180°) > $\dot{n}_i$ (ϕ = 0°), i.e., reverse flow. Also, the measurements show two relative maxima for $x_p \leq 30$ mm, indicating that more molecules are impacting the probe from the lateral direction. The two maxima cannot[47] be described by a local Maxwellian distribution function, but as shown in Ref. 47, they can be approximated remarkably well with an ellipsoidal distribution function along the flow centerline.

Both measurements and calculations show that a vortex forms for the most rarefied case (Condition 1) and increases in length with decreasing Knudsen number. These findings are consistent with the DSMC calculations[32] for the SR3 test conditions. Figure 23 presents calculated and measured results for test Condition 2 (P_0 = 5 bars), and illustrates good agreement for the wake centerline number flux, nu, ratioed to the free-stream flux, $(nV)_\infty$. The agreement is good in terms of both the extent of separation and the magnitude of the molecular fluxes. An obvious implication[47] is that the assumptions for the experimental data evaluation—no flow disturbance by the probe, free molecular flow about the probe, ratio of transmission probabilities equal to one—are sufficient to build a physical picture of the wake flow that is consistent with the DSMC calculations. The range of validity of these assumptions as well as the sensitivity of the numerical results to different DSMC models and calculation procedures should be investigated in future studies. Three-dimensional
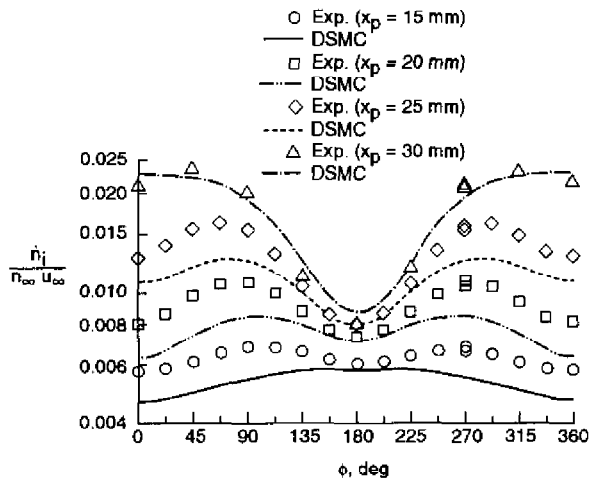

O   Exp. (x_p = 15 mm)
——   DSMC
□   Exp. (x_p = 20 mm)
—·—   DSMC
◇   Exp. (x_p = 25 mm)
·····   DSMC
△   Exp. (x_p = 30 mm)
—··—   DSMC

Fig. 22 Measured[45] and calculated[47] Patterson probe incident flux as a function of position and turning angle (ϕ = 0° denotes probe looking at model base plane).
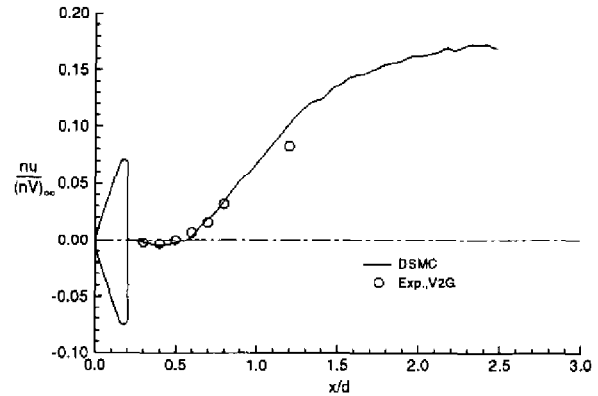

Fig. 23 Measured[45] and calculated[32] number flux along centerline of near wake for V2G test Condition 2.

simulations are essential to clarifying the impact of the probe-induced flow disturbance on the probe measurements.

5.2.3   HEG Tests and Computations

The HEG facility is a large free piston shock tunnel[48] that is capable of producing very high enthalpy gases. A series of experiments has been conducted in the HEG at the DLR, Göttingen, with a 70° spherically blunted cone having a base diameter of 15.24 cm. These tests have contributed to the high enthalpy, higher Reynolds number results of the WG 18 activity as discussed in Chapter IV. Legge[18] describes several tests that have been conducted in air with enthalpies of 10 to 23 MJ/kg at free-stream Mach numbers of approximately 10. For some of these tests, an array of four small models, 5 mm in diameter, were tested simultaneously with the larger model. The small models were located off centerline of the nozzle axis, as was the large model. Objectives of the small model tests were to assess different heating rate measurement techniques and obtain heating rate data at two locations along the forebody. Details concerning the experiments, models, and data reduction are given in Refs. 18 and 49. The estimated[18] error of the heat transfer measurements for the small cone tests is ± 25 percent. The scatter as shown in Ref. 18 is within ± 20 percent.

Reference 18 presents the free-stream conditions, including the free-stream gas composition as calculated with a one-dimensional nonequilibrium nozzle code for nine test conditions. Table 1 lists the free-stream conditions for two of these tests [shots 132 (Condition 1), and 131 (Condition 2)] for which DSMC calculations[32] have been made. The DSMC calculations were made using a 5-species reacting air gas model. For the lower enthalpy condition (Condition 1), the maximum mole fraction of atomic nitrogen behind the bow shock was of the order of 0.01, while the value for Condition 2 was of the order of 0.2. The calculated heating rate distributions for both cases are presented in Fig. 24 where the surface is assumed to be noncatalytic at a cold wall temperature of 300 K. Also shown are the measured results[18]
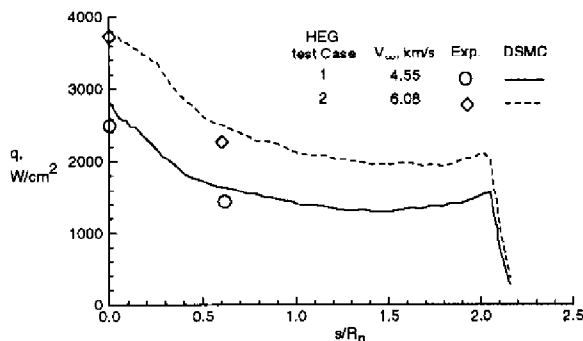
Fig. 24 Measured[18,49] and calculated[32] heating rates for two HEG tests using 5 mm base diameter models.

obtained by using the thin wall technique at the stagnation point and an s/R_n location 0.6. Good agreement is obtained for both shots concerning the distributions and absolute values.

For the mini cone tests in HEG, the free-stream Knudsen number is rather small, having values of .003 and .009 for the two conditions listed in Table 1; consequently, the effects of rarefaction on forebody heating should be minimal. This result is confirmed by the data analysis of Legge[18] that shows that the stagnation point heat transfer follows essentially a continuum behavior. Also, the heat transfer values at $s/R_n = 0.6$, when normalized by the stagnation value for the mini cones, fit well with the measurements of Kastell et al.[50] for the large models (d_b= 152.4 mm).

5.3 Calspan Tests (LENS)

Several series of experiments [16–17] have been conducted at Calspan with large (d_b = 15.24 cm) spherically blunted cone models. Tests were made in the Large Entry National Shock (LENS) facility using both nitrogen and air as test gases. Tests at 5 and 10 MJ/kg conditions for a range of reservoir pressure conditions (70 to 500 bars) have been completed where the models were sting-supported at zero incidence. Measurements consisted of surface pressure and heating rates along the forebody, base, and sting. The focus of these tests have been at continuum conditions; however, one test has been made at low pressure conditions where rarefaction effects should be evident in the wake. The specifics of this test condition, normally denoted as LENS test condition B, is listed in Table 1.

5.3.1 LENS Test Condition B and Computations

Details of the instrumentation which was concentrated along the sting are given in Ref. 16. Med-Therm coax gauges were installed on the front face of the model while magnesium fluoride-coated thin film heat transfer gages were employed on the base of the model and sting. The pressure transducers were piezoelectric sensors developed by Calspan. Special requirements for conducting the measurements at the current

test condition along with measurement uncertainties are summarized in Ref. 17.

Results of the experimental measurements for the low pressure test were first presented in Ref. 16 and more recently were included in Ref. 17. DSMC results for this test condition have been reported in Refs. 32, 39, and 51–54. Figures 25 and 26 present comparisons of calculated surface quantities for heating rate and pressure where the calculations were for nonreacting nitrogen. The DSMC results shown are those obtained by Moss[51] et al. using the DSMC method of Bird, while the Navier-Stokes results are those obtained by Hash[32], using an implicit, 3-temperature Navier-Stokes solver having the features discussed in Ref. 21–22. The slip boundary conditions used are those discussed in Ref. 55. The overall agreement between the DSMC and Navier Stokes calculations is shown to be good, particularly along the sting. Largest differences occur along the base plane. The implication of the present comparison is that a Navier-Stokes solver can provide an adequate prediction of surface quantities for the current test problem ($Kn_\infty = 0.002$).

Also shown in Figs. 25 and 26 are comparisons of measured and calculated values. As evident, there is generally good agreement between the calculations and measurements, both in the separated region and toward the end of the recompression process, indicating[16] that the size of the base flow region is well predicted. The calculations produce slightly higher values for pressure and heat transfer in the recompression region over the sting. The measurements for the forebody are very limited for this particular test in that pressure values initially reported[16] had to be discarded since the range of the pressure sensors was not appropriate for this test condition. With only two heat transfer measurements along the forebody, it is not possible to establish the experimental trend for heat transfer distribution. The DSMC and Navier-Stokes results are in close agreement along the forebody with differences less than 10 percent.
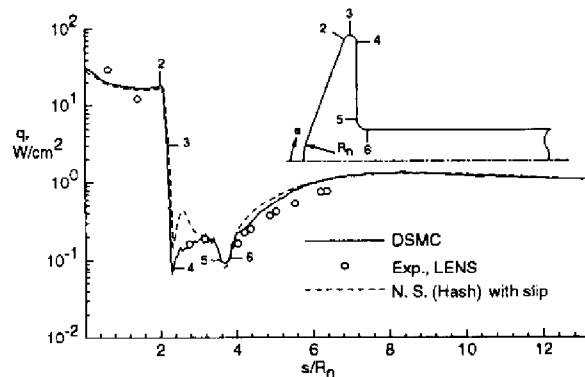

Fig. 25. Measured[16] and calculated[32] heating rate distributions for LENS test Condition 1 (Condition B).
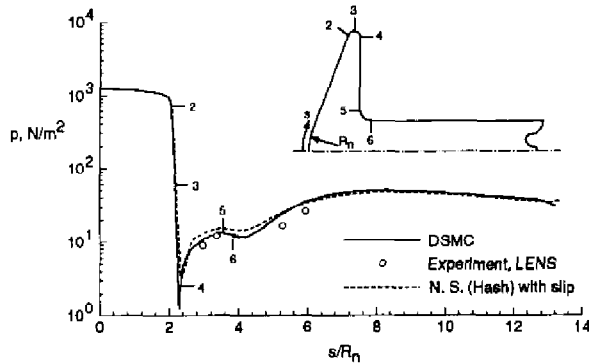
Fig. 26 Measured[16] and calculated[32] pressure distributions for LENS test Condition 1 (Condition B).

A summary of the DSMC[51] results for this test condition is as follows: 1) a wake vortex exists and extends 9 cm ($s/R_n = 6.0$) downstream of the base plane; 2) peak heating on the sting occurs downstream of the near wake stagnation point at $s/R_n = 8.4$, having a magnitude of 1.3 W/cm^2 or 4.2 percent of the forebody stagnation point value; 3) separation occurs on the outer corner before the surface becomes tangent to the base plane (just before location 4 in Fig. 25); 4) minimum values for surface pressure and heating rate occur at or near this location; 5) density in the near wake has a minimum value near the junction of the outer corner and base plane with a magnitude of about 20 percent of the free-stream value; and 6) small values for temperature jump and velocity slip are evident along the sting.

Other DSMC solutions obtained for this test condition are those of Gallis and Harvey[39,53] and Dietrich and Boyd[54]. In general, the agreement among the three DSMC solutions is good for surface quantities.

This test condition provides a valuable complement to the flow conditions that can be produced in low-density wind tunnels in that more energetic flows are produced. For the current condition, high temperature gas effects are present. That is, the nitrogen gas that envelops the test model is in thermal nonequilibrium; yet there is negligible dissociation.

5.3.2 LENS Test Conditions C and E and Computations

During the course of the WG18 activity, results from several DSMC computations have been published for free-stream Knudsen numbers of the order of 0.0001, flows well outside the focus of the present chapter. A few comments are appropriate since DSMC computations have been published for these conditions. A concern was the possible effects of rarefaction as the flow expands about the corner radius into the wake. Test conditions for which DSMC solutions have been reported are LENS conditions C[25,40] and E (Refs. 35 and Boyd in Ref. 17) and one[35] for the HEG series of tests (shot 132, listed as Condition 1 in Table 1) where the test model was the large sting-supported, spherically blunted cone ($d_b = 15.24$ cm). Details of the latter two test conditions are

given in Chapter IV. These tests were conducted in air. Test Condition C ($V_\infty = 3088.7$ m/s, $\rho_\infty = 4.247 \times 10^{-3}$ kg/m^3, $T_\infty = 226.3$ K, $M_\infty = 10.23$) was included as a rarefied test case in the 4th European High-Velocity Database Workshop, ESTEC, Noordwijik, Nov. 1994. Note that the free-stream density is 32.5 times that listed for LENS B or Condition 1 in Table 1. Therefore, the local mean free path throughout the computational domain for Condition C would be an order of magnitude smaller than that for Condition B. By using a typical engineering workstation, the computational resources are probably excessive to achieve a cell resolution that would ensure accurate heat transfer predictions for Condition C. Experience shows that when the computational cells adjacent to a surface are larger than the local mean free path, the calculated heating rates will be too high. This was the ESTEC Workshop experience where four reacting and one nonreacting DSMC submissions were made. The DSMC forebody heating results were much higher than the measured values and the same was true along the sting. Another concern expressed in Ref. 25 was the lack of convergence, particularly in the wake region, because of the longer time required to achieve steady flow. The best agreement between calculations and measurements was achieved with the one Navier-Stokes solution submitted by Hash[56] et al.

More recent DSMC computations (Refs. 35 and 36 and Boyd in Ref. 17) for these conditions have used a zonally decoupled (forebody solved using Navier-Stokes and the wake using DSMC) approach (discussed earlier for the SR3 test conditions) or a hybrid[37] DSMC/Navier-Stokes approach. Even with the these computational approaches, which achieve a substantial reduction in computational cost as compared to a full DSMC simulation, the computational requirements are still substantial. In fact, the solutions of Hash and Hassan[36-37] and Gochberg[35] et al. indicate deficiencies (cells too large or cells not adequately populated). Consequently, a convincing case has not been made that rarefaction effects are significant or that DSMC would enhance the computational results for the blunt body/wake problems where Kn_∞ is of the order of 10^{-4}.

5.4 Flight Entry Test Conditions

The flight test cases consist of four individual cases to provide code-to-code comparisons for a 70° spherically blunted cone 2 m in diameter and flat along the afterbody. No experimental results are available for these test cases. The test cases are for both Earth and Mars entry using both reacting and nonreacting gas models. The free-stream and surface boundary conditions are specified in Ref. 1 and listed in Table 2. These conditions correspond to altitudes of approximately 85 and 68 km in the Earth and Mars atmospheres, respectively. Consequently, both the model size and entry conditions are representative of current planetary missions. The combination of high velocity and relatively low free-stream Knudsen numbers ($Kn_\infty \approx 0.003$) ensures substantial forebody dissociation. Key interest was the impact of nonequilibrium chemical activity along the forebody and

the combined effects of rarefaction and chemical activity in the near wake.

5.4.1 Earth Reentry

Dogra[57] et al. presented results for both reacting and nonreacting air test cases calculated with the DSMC method of Bird and also reacting air solutions using an axisymmetric 3-temperature, 5-species implicit Navier-Stokes solver described in Refs. 21 and 22. The DSMC and Navier-Stokes results were in close agreement for the wake flow-field quantities. Also, the size of the vortex, as measured from the base of the blunted cone to the wake stagnation point, is identical $(0.77 \, d_b)$ for the two solutions. Both solution methods indicate that the air dissociation is significant for the current flow conditions. Near the forebody surface, essentially all the molecular oxygen and over half of the molecular nitrogen species are dissociated (noncatylatic wall assumption). Species separation among the heavy (N_2) and light $(O$ and $N)$ species was evident in the DSMC results as the flow expanded into the wake region. This separation produces some differences in the wake chemical composition where a larger concentration of atomic species was evident in the near wake for the DSMC solution. As for the surface heating results (Fig. 27), both methods are in good agreement along the forebody. Along the base plane, the Navier-Stokes heating values results exceeds the DSMC results by 25 percent or more with a maximum difference of 200 percent aft of the corner expansion.

When the calculation is made assuming nonreacting chemistry, as was done in Ref. 57, then the DSMC results, compared with the reacting air solution, shows much higher surface heating rates—49 percent higher at the forebody stagnation point and about 240 percent higher along the base; a smaller wake vortex $(0.62 \, d_b)$; similar values for the wake density contours; and essentially the same value for drag. If
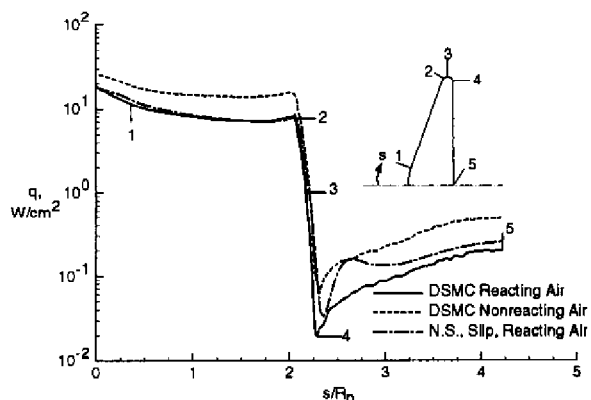

Fig. 27. Calculated[57] heating rate distributions for Earth reentry (Alt = 85 km, V_∞ = 7.0 km/s, d_b = 2.0 m, R_n = 0.5 m).

the reacting gas calculations had been made with a finite or fully catalytic surface boundary condition, then the difference in surface heating would have been less.

DSMC solutions along the forebody were also reported by Gallis and Harvey[58] for this test case, in which a different model for the nonequilibrium chemistry is used compared to that of Ref. 57. Reacting and nonreacting results are presented showing the effect of the chemistry on stagnation temperature and density profiles, but not on heating rates. The reacting heating rate results are somewhat higher, particularly in the stagnation region, when compared to that of Ref. 57.

Additional DSMC solutions related to this test condition have been reported. Dogra[57] et al. also examined the effect of including two afterbody configurations: (1) a cylindrical afterbody (cylinder diameter = 0.5 d_b) and 2) a conical frustrum (similar to the Mars Pathfinder afterbody). Details of the effect on flow-field features and surface heating are discussed. As was the case for the DSMC calculations made for the SR3 wind tunnel conditions, the presence of an afterbody had no effect on the forebody flow field or surface quantities. Dogra[59] et al. examined the effect of rarefaction on the wake structure by calculating the flows for altitudes of 75, 85, 95, and 105 km at the same free-stream velocity and surface boundary conditions, but for the Mars Pathfinder Probe $(d_b = 2.65$ m). Three-dimensional DSMC calculations have been presented by Celenligil[60,61] where the only modification was that the free-stream conditions were for an altitude of 90 km; hence a more rarefied condition where $Kn_\infty \approx 0.0085$. The calculation used the DSMC method of Bird and a reacting five species air gas model. Results for zero incidence are discussed in Ref. 60, while those for 10°, 20°, and 30° incidence are presented in Ref. 61. Results show the presence of a wake vortex for all cases considered. Reference 61 presents details of calculated surface, flow field, and aerodynamic results.

5.4.2 Mars Entry

Previous studies addressing chemical reactions and rarefaction effects for Mars entry are relatively few. DSMC studies by Hash and Hassan[62] and Gallis and Harvey[63] are examples of stimulations that address the chemical and fluid relaxation issues associated with blunt body entries where the free stream consists primarily of CO_2. One contribution[64] has been reported for the Mars test conditions (Table 2) and one closely related contribution[63]. Those of Moss[64] et al. were done for both reacting and nonreacting CO_2/N_2 flows using the DSMC method of Bird[11] with the chemical reaction set (9 species) based on the data of Hash and Hassan[62]. The calculations of Gallis and Harvey used the maximum entropy method for simulating the chemical reactions and energy exchange. The later calculations are only for the forebody and were conducted at a free-stream density equal to 72.7 percent of the test case value.

Examples of the results obtained from the calculations by Moss[64] et al. are presented in Figs. 28 through 29 showing the effect of chemical reactions on flow field and surface results. Several calculations were made to refine the grid to achieve a cell spacing normal to the surface that is less than the local mean free path. Flow-field features as influenced by chemical reactions are presented in Figs. 28(a) and 28(b) where the density contours and particle traces are shown, respectively. As was shown for the Earth reentry results[57], the flow with reacting chemistry has a larger wake vortex than the nonreacting results. Unlike the Earth entry test case results, there are larger differences in the near wake density contours for the reacting and nonreacting calculations. For the reacting calculation, the gas species adjacent to the surface are
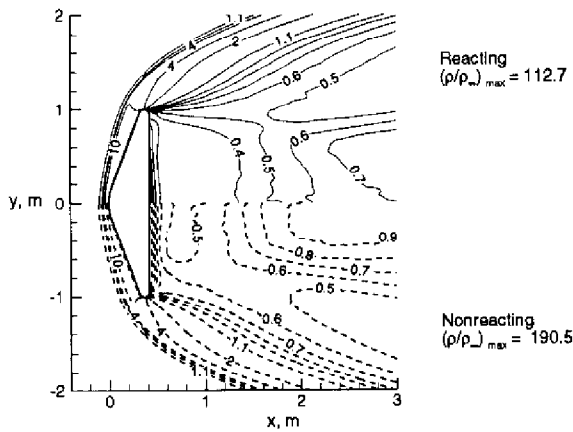
(a) Density contours, ρ/ρ_∞, where $\rho_\infty = 1.187 \times 10^{-5}$ kg/m^3.
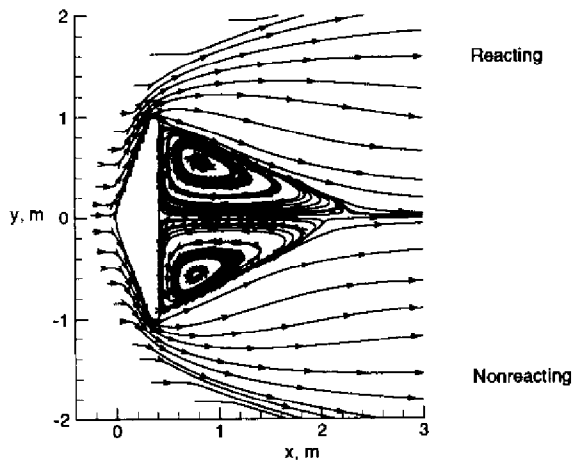
(b) Particle traces.

Fig. 28 DSMC Calculated[64] effects of nonequilibrium chemistry on flow-field quantities for Mars entry (Alt = 68 km, V_∞ = 7.0 km/s, d_b = 2.0m, R_n= 0.5 m).
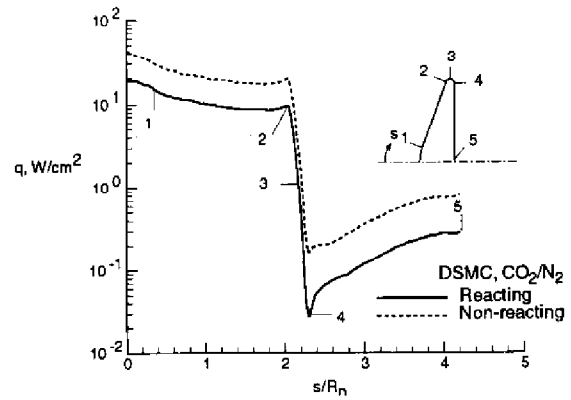

Fig. 29. Calculated[64] heating rate distributions for Mars entry (Alt = 68 km, V_∞ = 7.0 km/s, d_b = 2.0 m).

predominantly CO and atomic oxygen. In the near wake, the calculated mole fractions for atomic oxygen and CO are approximately 0.50 and 0.45, respectively.

With essentially all of the CO_2 being dissociated over the forebody, the surface heating to a noncatalytic wall is substantially less than the nonreacting solution. At the stagnation point, the nonreacting value was 2.1 times the reacting value while along the base plane the nonreacting value was 2.9 times (at y = 0.5 m) the reacting value. As was the case for Earth re-entry, the impact of chemistry on the drag coefficient was insignificant. The calculated drag coefficient was 1.65 for the reacting solution where the pressure contribution to the total drag was 98.8 percent.

Gallis and Harvey[63] presented forebody solutions with and without chemical reactions for the Mars entry conditions except that the free-stream density was less than the test condition. Consequently, their dimensional heating values would be lower than that for the test conditions. However, their calculated heating values are greater by a factor of two or more than the results shown in Fig. 29 for both the reacting and nonreacting cases. Their heating results appear excessively high based on stagnation engineering correlations or viscous-shock-layer results. For the Mars test condition, the stagnation engineering correlation of Sutton and Graves[65] gives a value of 32 W/cm^2 assuming chemical equilibrium. A 16-species nonequilibrium reacting gas model as implemented in the viscous-shock-layer analysis of Gupta[66] gives a stagnation value of 22.9 W/cm^2. The heating results presented in Fig. 29 are believed to be more realistic based on the correlation and viscous-shock-layer results than the results presented in Ref. 63.

Additional calculations are needed for the generic flight test cases, particularly the Mars test case, to assess the differences among solution methods as well as the modeling issues

associated with thermal and chemical nonequilibrium. Solutions, with and without chemical reactions, help to isolate differences that might exist among solutions. A critical discriminator is the surface heating.

6 FINDINGS AND RECOMMENDATIONS

6.1 Corner-Flow/Jet Interaction Problem

Calculations performed by different workers on the corner flow / jet interaction problem reproduce qualitatively the features of the pressure distributions obtained experimentally. However, quantitative agreement was not achieved. Also small differences between calculated results were observed.

The potential sources of discrepancies between results have been examined. Differences in implementing the numerical methods (e.g., boundary conditions, gas modeling, discretization) can explain small differences but not large ones.

It is suggested that additional experiments be conducted to clarify other potential causes of discrepancies:

• Measure the jet mass flow rate.

• Measure the wall temperature (and examine its influence on measured pressure).

• Confirm the absence (or not) of condensation in the jet.

• Scan or visualize the flow field (e.g., using the electron beam fluorescence technique) to obtain a better understanding of the shape of the jet and of the boundary conditions to use, particularly along the upper boundary.

6.2 Blunt-Body/Wake-Closure

A key aspect of the success of this activity has been the experimental contributions from five hypersonic facilities that have fostered a significant number of computational contributions. The experiments have provided heating and aerodynamic data and previously unavailable data as to the features of the wake flow structure and how these quantities are influenced by rarefaction. Application of DSMC and Navier-Stokes methods to many of the test conditions have provided insight and confidence on where the methods can be effectively applied to such problems. The synergy of the computational/experimental activities has produced a significant database that can serve as a valuable aid for validation purposes as well as an aid for aerobraking and planetary probe mission designs. Some of the key contributions or findings of this activity are 1) first experimental measurements of wake density field and number flux for generic Aeroassist Space Transfer Vehicle configuration; 2) database involving both quantitative and qualitative information that spans a wide range of conditions (nonreacting to reacting flows) in the transitional regime; 3) demonstrated capability of different DSMC codes to simulate selected test cases (SR3, Condition 2); 4) the

experimental (V2G, Patterson probe) and computational findings which show that a vortex is established when there is a strong non-Maxwellian distribution function in the wake and the size of the wake vortex increases with decreasing Knudsen number; 5) the maximum heating along a sting/afterbody for zero incidence was of the order of five percent of the forebody stagnation value; 6) the location of wake reattachment and maximum sting heating rate are not coincident, and the separation between the two locations diminishes with decreasing rarefaction; 7) inclusion of slip boundary conditions in the Navier-Stokes solvers provided improved agreement with experimental and DSMC results; 8) results from the Navier-Stokes solutions suggest that the overall Knudsen number should be of the order of 0.001 or less before good agreement is achieved between experiment or DSMC for the near wake surface and flow features, and that the Navier-Stokes solutions agree with the DSMC results for quite large overall Knudsen numbers along the forebody; 9) the combined use of Navier-Stokes for the forebody with a decoupled DSMC solution for the wake provides an efficient method for solving transitional blunt-body flows where the forebody flow is continuum and the wake is rarefied; and 10) for the generic flight test cases which involve substantial dissociation, the calculated forebody and afterbody heating for the reacting solutions are substantially less than for the corresponding nonreacting cases.

Additional experiments and computations should be carried out to address discrepancies and areas of uncertainties:

• generation of a more extensive experimental heating rate distribution data base with contributions from multiple facilities using the same test model when possible (wakes with laminar free shear layers including sting reattachment are essential data for computational tool benchmaking)

• parametric DSMC studies demonstrating the sensitivity of flow-field and surface results to the models implemented regarding internal energy exchange and nonequilibrium chemistry for generic flight test conditions

• parametric studies using Navier-Stokes solvers with surface slip and temperature jump boundary conditions to examine the sensitivity of calculated wake flow-field and surface results to grid (both density and alignment) and code dissipation for free-stream Knudsen numbers of the order of 10^{-3}

• three-dimensional DSMC simulations to complement the Patterson probe measurements and provide more insight as to potential interference effects of the intrusive measurements

REFERENCES

1. Hypersonic Experimental and Computational Capability, Improvement and Validation," edited by Saric, W. S., Muylaert, J., and Dujarric, C., AGARD AR-319 Vol.1, May 1996.

2. Allègre, J. and Raffin, M., "Experimental Study on Control Jet Interaction," Laboratoire d'Aérothermique du CNRS, Report RC 91-11, 1991.

3. Allègre, J. and Raffin, M., "Experimental Study on Control- Jet/Corner-Flow Interaction," Laboratoire d'Aérothermique du CNRS, Report RC 92-7, 1992.

4. Allègre, J., and Raffin, M., "Control Jets Interacting with Rarefied Hypersonic Flows," 72nd Fluid Dynamics Panel Symposium on Computational and Experimental Assessment of Jets in Cross Flows, Winchester, UK, April 19–22, 1993.

5. Chauvot, J. F., Dumas, L. and Dupuis, D., "Corner flow jet interaction: computation and experiment," Rarefied Gas Dynamics 19, edited by J. Harvey and G. Lord, Oxford University Press, 1995, pp. 773–779.

6. Hendriadi, R., "Etude de simulation numérique d'un Écoulement hypersonique de gaz raréfié limité par deux plans perpendiculaires avec jet transversal," Laboratoire d'Aérothermique du CNRS, rapport de stage RS 93-3 (in French), 1993.

7. Tartabini, P. V., Wilmoth, R. G. and Rault, D. F. G., "Direct Simulation Monte Carlo Calculation of a Jet Interaction Experiment," Journal of Spacecraft and Rockets, Vol. 32, No 1, Jan.–Feb., 1995, pp.75–83.

8. Tartabini, P. V.,Wilmoth, R. G. and Rault, D F. G., "A systems approach to a DSMC calculation of a control jet interaction experiment," AIAA Paper 93-2798, 1993.

9. Wilmoth, R. G. and Tartabini P. V., "Three-Dimensional DSMC Calculations of Jet/Corner Flow Interactions," Rarefied Gas Dynamics 19, edited by J. Harvey and G. Lord, Oxford University Press, 1995, pp. 1209–1215.

10. Spear, A. J., Freeman, D. C. and Braun, R. D., "Mars Pathfinder Status at Launch," IAF- 96-Q.3.02, 47th International Astronautical Congress, Oct. 1996.

11. Bird, G. A., "Molecular Gas Dynamics and the Direct Simulation of Gas Flows," Clarendon Press, Oxford, 1994.

12. Bird, G. A., "Definition of a Mean Free Path for Real Gases," Phys. of Fluids, Vol.26, 1983, pp. 3222–3223.

13. Potter, J. L. and Blanchard, R. C., "Thermomolecular Effect on Pressure Measurements with Orifices in Transitional Flows," Rarefied Gas Dynamics, edited by A.E. Beylich, VCH, 1991, pp. 1459–1465.

14. Cline, M. C., "VNAP2: A Computer Program for Computation of Two-Dimensional, Time-Dependent, Compressible, Turbulent Flow," Los Alamos Scientific Laboratory, LA-8872, Los Alamos, NM, Aug. 1981.

15. Lengrand, J.C., Raffin, M. and Allègre, J., "1981 Monte Carlo Simulation Method Applied to Jet-Wall Interactions under Continuum Flow Conditions," Rarefied Gas Dynamics, Sam.S.Fisher ed., Progress in Astronautics and Aeronautics, Vol.74, 1981, pp.994–1006.

16. Holden, M., Kolly, J. and Chadwick, K., "Calibration, Validation, and Evaluation Studies in the LENS Facility," AIAA Paper 95-0291, Jan. 1995.

17. Holden, M., Harvey, J., Boyd, I., George, J., and Horvath, T., "Experimental and Computational Studies of the Flow Over a Sting Mounted Planetary Probe Configuration," AIAA Paper 97-0768, Jan. 1997.

18. Legge, H., "Experiments on a 70 Degree Blunted Cone in Rarefied Hypersonic Wind Tunnel Flow," AIAA Paper 95-2140, June 1995.

19. Gnoffo, P. A., "An Upwind-Biased, Point-Implicit Relaxation Algorithm for Viscous Compressible Perfect-Gas Flows," NASA TP-2953, February 1990.

20. Gnoffo, P. A., Gupta, R. N. and Shinn, J. L., "Conservation Equations and Physical Models for Hypersonic Air Flows in Thermal and Chemical Nonequilibrium," NASA TP-2867, Feb. 1989.

21. Olynick, D. R. and Hassan, H. A., "New Two-Temperature Dissociation Model for Reacting Flows," Journal of Thermophysics and Heat Transfer, Vol. 7, No. 4, Oct.–Dec. 1993, pp. 687–696.

22. Olynick, D. R., Taylor, J. C. and Hassan, H. A., "Comparisons Between DSMC and the Navier-Stokes Equations for Reentry Flows," AIAA Paper 93-2810, July 1993.

23. Allègre, J. and Bisch, D., "Blunted Cone at Rarefied Hypersonic Conditions— Experimental Density Flow-fields, Heating Rates, and Aerodynamic Forces," CNRS Report RC 95-2, September 1995.

24. Allègre, J., Bisch, D. and Lengrand, J.C., "A 70° Blunted Cone at Rarefied Hypersonic Conditions," submitted to Journal of Spacecraft and Rockets, 1997.

25. Coron, F. and Harvey, J. K., "Synopsis for Test Case 6— Rarefied 70° Spherically Blunted Cone," 4th European High-Velocity Database Workshop, ESTEC, Noordwijk, The Netherlands, Nov. 1994.

26. Moss, J. N., Mitcheltree, R. A., Dogra, V. K. and Wilmoth, R. G., "Direct Simulation Monte Carlo and Navier-Stokes Simulations of Blunt Body Wake Flows,"

AIAA Journal, Vol. 32, No. 7, 1994, pp. 1399–1406; also AIAA Paper 93-2807, July 1993.

27. Wilmoth, R. G., Mitcheltree, R. A., Moss, J. N. and Dogra, V. K., "Zonally Decoupled Direct Simulation Monte Carlo Solutions of Hypersonic Blunt-Body Wake Flows," *Journal of Spacecraft and Rockets*, Vol. 31, No. 6, Nov. – Dec. 1994, pp. 971–979; also AIAA Paper 93-2808, July 1993.

28. Marriott, R. M. and Bartel, T. J., "Comparison of DSMC Flow Field Predictions using Different Models for Energy Exchange and Chemical Reaction Probability," *Rarefied Gas Dynamics 19*, edited by J. Harvey and G. Lord, Oxford University Press, 1995, pp. 413–419.

29. Gilmore, M. R., "Rarefied Flow Over a Blunt Body," DRA/DWS/WX7/TR 95 189, February 1995.

30. Pallegoix, J. F., "Workshop ESTEC—Test Case No. 6—Rarefied Spherically Blunted Cone," Paper presented at 4th European High-Velocity Database Workshop, ESTEC, Noordwijk, The Netherlands, Nov. 1994.

31. Moss, J. N., Dogra, V. K. and Wilmoth, R. G., "DSMC Simulations of Mach 20 Nitrogen Flows about a 70° Blunted Cone and its Wake," NASA TM-107762, August 1993.

32. Moss, J. N., Dogra, V. K., Price, J. M. and Hash, D. B., "Comparison of DSMC and Experimental Results for Hypersonic External Flows," AIAA Paper 95-2028, June 1995.

33. Nance, R. P., Wilmoth, R. G., and Hassan, H. A., "A Comparison of Grid-Definition Schemes for DSMC," AIAA Paper 96-0604, Jan. 1996.

34. Dogra, V. K., Moss, J. N., and Price, J. M., "Near Wake Structure for a Generic ASTV Configuration," Journal of Spacecraft and Rockets, Vol. 31, No. 6, Nov.-Dec. 1994, pp.953-959; also AIAA Paper 93-0271, Jan. 1993.

35. Gochberg, L. A., Allen, G. A., Gallis, M. A., and Deiwert, G. S., "Comparison of Computations and Experiments for Nonequilibrium Flow Expansions Around a Blunted Cone," AIAA Paper 96-0231, Jan. 1996.

36. Hash, D. B., and Hassan, H. A., "A Decoupled DSMC/Navier-Stokes Analysis of a Transitional Flow Experiment," AIAA Paper 96-0353, Jan. 1996.

37. Hash, D. B., and Hassan, H. A., "Two-Dimensional Coupling Issues of Hybrid DSMC/Navier-Stokes Solvers," submitted for publication, Journal of Thermophysics and Heat Transfer, 1997.

38. Legge, H., "Heat Transfer and Forces on a Blunted 70 Deg. Half Angle Cone Measured in Hypersonic Free Jet Flow," DLR Report IB 222-93 A 33, November 1993.

39. Gallis, M. A. and Harvey, J. K., "Validation of DSMC Computations for the Flow-field Around a 70° Blunted Cone," *Rarefied Gas Dynamics 19*, edited by J. Harvey and G. Lord, Oxford University Press, 1995, pp. 1284–1290.

40. Gallis, M. A. and Harvey, J. K., "Comparison of the Maximum Entropy DSMC Code with Flow-field Measurements," AIAA Paper 95-0413, Jan. 1995.

41. Koura K. and Matsumoto H., Variable Soft Sphere Molecular Model for Inverse-Power-Law or Lennard Jones Potentials, Physics of Fluids A, Vol. 3, No. 10, pp. 2459–2465.

42. Legge, H., Nanbu, K. and Igarishi, S., "Force and Heat Transfer on a Disc in Rarefied Flow," Rarefied Gas Dynamics, edited by A. E. Beylich, VCH, 1991, pp. 679-686.

43. Celenligil, M. C. and Moss, J. N., "Hypersonic Rarefied Flow About a Delta Wing—Direct Simulation and Comparison with Experiment," AIAA Journal, Vol. 30, No. 8, August 1992, pp. 2017-2023.

44. Legge, H., "Flow Visualization and Pitot Probe Measurements in Hypersonic Rarefied Flow Around a 70 Deg. Half Angle Cone," DLR Report IB 223-95 A 01, February 1995.

45. Legge, H., "Patterson Probe Measurements in the Wake of a 70 Deg. Half Angle Cone in Hypersonic Rarefied Flow," DLR Report-IB 223-94 A 15, December 1994.

46. Legge, H., von Roden, G., Klotzbach, A. and Rammenzwieg, D., "Calibration Data of V2G with a Conical Ma = 15 Nozzle," DLR IB 223-94A 11, 1994.

47. Danckert, A. and Legge, H., "Experimental and Computational Wake Structure Study for a Wide-Angle Cone," Journal of Spacecraft and Rockets, Vol. 33, No. 4, 1996, pp. 476–482; also AIAA Paper 95-2141, June 1995.

48. Eitelberg, G., McIntyre, T., Beck, W., and Lacey, J., "The High Enthalpy Shock Tunnel in Göttingen," AIAA Paper 92-3942, 1992.

49. Legge, H., Rammenzweig, D. and Klotzbach, A., "Heat Transfer Measurements on a Blunted 70 Deg Half Angle Cone in High Enthalpy Small Reynolds Number Flow," DLR Report IB 223-95 A 22, March 1996.

50. Kastell, D., Horvath, T. J., and Eitelberg, G., "Nonequilibrium Flow Expansion Experiment Around a Blunted Cone," Paper presented at the 2nd European Symposium on Aerothermodynamics for Space Vehicles," Noordwijk, Netherlands, November 1994.

51. Moss, J. N., Price, J. M. and Dogra, V. K., "DSMC Calculations for a 70° Blunted Cone at 3.2 km/s in Nitrogen," NASA TM-109181, January 1995.

52. Moss, J. N. and Price, J. M., "Review of Blunt Body Wake Flows at Hypersonic Low Density Conditions," AIAA Paper 96-1803, June 1996.

53. Gallis, M. A. and Harvey, J. K., "Comparison of the Maximum Entropy DSMC Code with Flow-field Measurements," AIAA Paper 95-0413, Jan. 1995.

54. Dietrich, S. and Boyd, I. D., "Scalar and Parallel Optimized Implementation of the Direct Simulation Monte Carlo Method," Journal of Computational Physics 126, Vol. 126, 1996, pp. 328–342.

55. Gupta, R. N., Scott, C. D. and Moss, J. N., "Slip-Boundary Equations for Multicomponent Nonequilibrium Airflow," NASA TP-2452, Nov. 1985.

56. Hash, D. B., Hassan, H. A., Dogra, V. K. and Price, J. M., "Navier-Stokes Calculations for a Spherically Blunted Cone-LENS Condition," Fourth European High-Velocity Database Workshop, ESTEC, Noordwijk, Nov. 1994.

57. Dogra, V. K., Moss, J. N., Wilmoth, R. G., Taylor, J. C., and Hassan, H. A., "Effects of Chemistry on Blunt-Body Wake Structure," AIAA Journal, Vol. 33, No. 3, 1995,

58. Gallis, M. A. and Harvey, J. K., "Implementation of a Maximum Entropy Method in Monte Carlo Direct Simulations," AIAA Paper 95-2094, June 1994.

59. Dogra, V. K., Moss, J. N., Wilmoth, R. G., Taylor, J. C., and Hassan, H. A., "Blunt Body Rarefied Wakes for Earth Entry," Journal of Thermophysics and Heat Transfer, Vol. 9, No. 3, July–Sept., 1995, pp. 464–470; also AIAA Paper 93-0271, Jan. 1993.

60. Celenligil, M. C., "Three-Dimensional Wake Flow Simulations for a 70-deg Blunted Cone During Re-Entry," Rarefied Gas Dynamics 19, edited by J. Harvey and G. Lord, Oxford University Press 1995, pp. 1140–1146.

61. Celenligil, M. C., "Rarefied Wake Flow Simulation for a 70-deg Blunted Cone at Incidence," 20th International Symposium on Rarefied Gas Dynamics, Beijing, China, August 1996.

62. Hash, D. B. and Hassan, H. A., "Monte Carlo Simulation of Entry in the Martian Atmosphere," Journal of Thermophysics and Heat Transfer, Vol. 7, No .2, April-June 1993, pp. 228–232.

63. Gallis, M. A. and Harvey, J. K., "Analysis of Non-Equilibrium in Mars Atmosphere Entry Flows," AIAA Paper 95-2095, June 1995.

64. Moss, J. N., Wilmoth, R. G. and Price, J. M., "DSMC Simulations of Blunt Body Flows for Mars Entries," AIAA Paper 97-2508, June 1997.

65. Sutton, K. and Graves, R. A., "A General Stagnation-Point Convective-Heating Equation for Arbitrary Gas Mixtures," NASA TR-376, Nov. 1971.

66. Gupta, R. N., Lee, K. P. and Scott, C. D., "Aerothermal Study of Mars Pathfinder Aeroshell," Journal of Spacecraft and Rockets, Vol. 33, No. 1, Jan.–Feb. 1996, pp. 61–69.